[1]

[Introduction to Surface-Mount Technology]

[Oliver Krammer]

[Department of Electronics Technology, Budapest University of Technology and Economics]

Abstract: In chapter 1, the surface-mount technology and reflow soldering technology are overviewed. A brief introduction is presented into the type of electronic components, including through-hole- and surface-mounted ones. Steps of reflow soldering technology are outlined, and details are given regarding the properties of solder material in this technology. The rheological behavior of solder pastes is detailed, and some recent advancements in addressing the thixotropic behavior of this material are summarized. The process of stencil printing is detailed next, which is the most crucial step in reflow soldering technology; since even 60–70% of the soldering failures can be traced back to this process. The topic includes the structures of stencils, discussion of the primary process parameters, and process optimization possibilities by numerical modeling. Process issues of component placement are presented. The critical parameter (process and machines capability), which is used extensively for characterizing the placement process is studied. In connection with the measurement of process capability, the method of Gage R&R (repeatability and reproducibility) is detailed, including the estimation of respective variances. Process of the reflow soldering itself is detailed, including the two main phenomena taking place when the solder is in the molten state, namely: wetting of the liquid solder due to surface tension, and intermetallic compound formation due to diffusion. Solder profile calculation and component movements during the soldering (e.g., self-alignment of passive components) are presented too. Lastly, the pin-in-paste technology (reflow solder of through-hole components) is detailed, including some recent advancements in the optimization of this technology by utilizing machine learning techniques.

Key Words: surface-mount technology; reflow soldering; component skewing and self-alignment; stencil printing; numerical simulation; machine- and process capability; pin-in-paste technology.

[1.1 Electronic components]

Today electronic circuits consist of almost solely surface-mounted components (~90%) and potentially only some through-hole components for realizing plug connectors or high power devices. Surface-mounted components and surface-mount technology are evolving since the mid-1960s [1.1]. Nowadays, the pitch dimensions reduced down to 0.3 mm or to even lower by the interest of portable device manufacturers, for example. Nevertheless, surface-mounted components never can supersede the through-hole devices entirely; therefore, the assembly of both types of components should be done by the comprehensive soldering technology, which is reflow soldering.

The electronic components can be classified from many points of view, e.g., they can be passive or active components or electromechanical components like switches, connectors, or relays. From the assembly point of view, the components can be through-hole (Fig. 1.1) or surface-mounted (Fig. 1.2). From the packaging point of view, they can be discrete components (one function is realized by one component – e.g., a resistor), they can be packaged as series of alike components (e.g., resistor array), or can be integrated components, in which many functions are realized by one component.

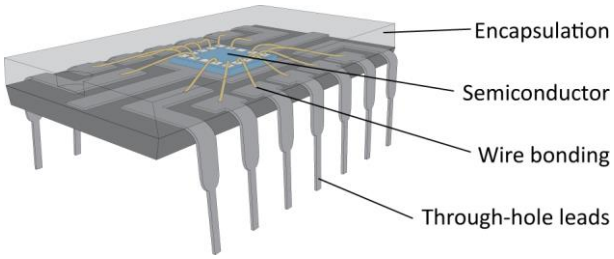

*** Insert Figure 1.1 ***

Caption: 1.1. Through-hole integrated circuit – dual inline package (DIP)

Credit: [1.2]

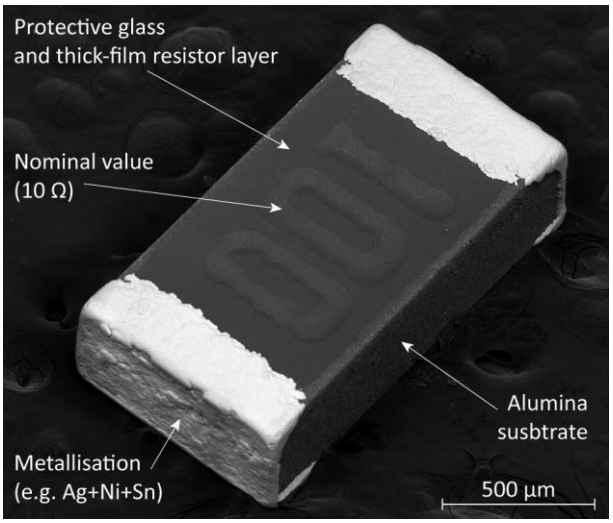

*** Insert Figure 1.2 ***

Caption: 1.2. Scanning electron microscopy image of a surface-mounted resistor

Credit: –

In this chapter, the different types of electronic components will be detailed. Classification possibilities will be elaborated for both through-hole and surface-mounted components. Finally, the advantages and disadvantages of both through-hole and surface-mount technology will be given and compared to each other.

[1.1.1 Through-hole components]

The through-hole (TH) components can have flexible or rigid/fixed leads. The flexible leads are bent according to the position of the holes in the printed wiring board (PWB) and cut to the proper size. In the case of TH components with rigid leads, the through-holes in the PWB are designed according to the position of the leads in a given raster. In through-hole technology (THT), component leads are inserted through the holes of the printed wiring board, and they soldered to the lands (solder ring) on the other side

of the PWB. Therefore, a TH assembly has a ′component side′ and a ′soldering side′ (Fig. 1.3).

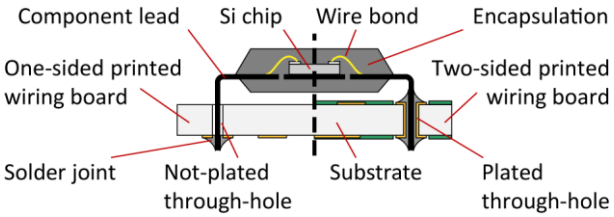

*** Insert Figure 1.3 ***

Caption: 1.3. Schematic of a soldered through-hole component; formation of solder joint in the case of not-plated through-holes (left side) and plate through-holes (right side)

Credit: [1.2]

The arrangement of the component leads can be axial (resistors, capacitors), radial (transistors, LEDs – light-emitting diodes), or the leads can be in the so-called perimeter style, where the leads are located in the perimeter of the components along its edges (integrated circuit packages). Further, special through-hole components are the high lead-count, PGA (pin grid array) packages (e.g., CPUs in personal computers in the 1990s), and the electromechanical components, like USB connectors. In PGA packages, the leads are located in a so-called grid array style, where a grid is projected onto the bottom side of a package, and the leads are at points of intersections. The advantage of these types of components is that they can be placed into sockets with detachable mechanical joining, which makes it possible to change the components easily.

The through-hole components are stored according to the type of component as follows: axial lead components are stored in two-sided straps; radial lead components are stored in single-sided straps; whereas integrated circuit packages are stored in tube/stick

magazines. All of them aid the automated placement of components, which includes the following steps for axial- and radial lead components:

- Cutting out the component from the strap, in which it is placed in the proper order
- Picking the component up, bending its leads for the right shape, then positioning both the component and the bending unit
- Inserting the component into the holes of the printed wiring board, cutting the leads of the component
- Fixing the components by bending back its leads on the bottom side of the PWB

High current capacity and high mechanical strength of the connections are the advantages of through-hole technology. Disadvantages include the large area occupied on both sides of the PWB by the components, and the automated insertion becomes problematic if the lead count of the component is large (>40). Furthermore, the package shapes of through-hole components are not standardized exhaustively.

[1.1.2 Surface-mounted components]

The surface-mounted components are placed and joined (e.g., soldered) directly to the surface of the printed wiring board. They have short leads, which are inappropriate for through-hole mounting, or they have no leads at all, just solderable, metalized terminals on the sides or the bottom of the package. The copper pattern (footprint) on the printed wiring board is designed according to the geometrical layout of components' terminals. Regularly, the components are placed onto the soldering pads, and they are soldered on the same side (Fig. 1.4).

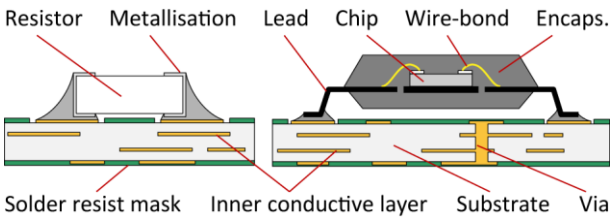

*** Insert Figure 1.4 ***

Caption: 1.4. Schematic of soldered surface-mounted components

Credit: [1.2]

The most widely used passive components are the thick-film surface-mounted resistors and the ceramic (layer) capacitors. A size code describes the size of the components – designation e.g., 1206 –, which indicates the length and the width of the component by the following rule (down to 0402): 12·10 = 120 mil; 06·10 = 60 mil, where the mil is milliinch, the thousandth of an inch (0.001″, 25.4 μm). Regular size codes are collected in Table 1. The surface-mounted passive components are stored in paper- or plastic tapes.

*** Insert Table 1.1 ***

Caption: 1.1. Regular size codes of surface-mounted passives

Credit: [1.2]

Designation	**L × W [mil]**	**L × W [mm]**
1206	120 × 60	3.2 × 1.6
0805	80 × 50	2 × 1.2
0603	60 × 30	1.6 × 0.8
0402	40 × 20	1 × 0.5
0201	24 × 12	0.6 × 0.3
01005	16 × 08	0.4 × 0.2
0201m	10 × 5	0.25 × 0.12
0201mm	8 × 4	0.2 × 0.1

The active and integrated surface-mounted components can be classified according to the arrangement of the leads similar to the through-hole components. Integrated component packages with perimeter style leads include SOT (small outline transistor), SOIC (small outline integrated circuit – Fig. 1.5), QFP (quad flat pack), PLCC (plastic leaded chip carrier) packages. Both the QFP and PLCC packages have leads on all four sides of the component.

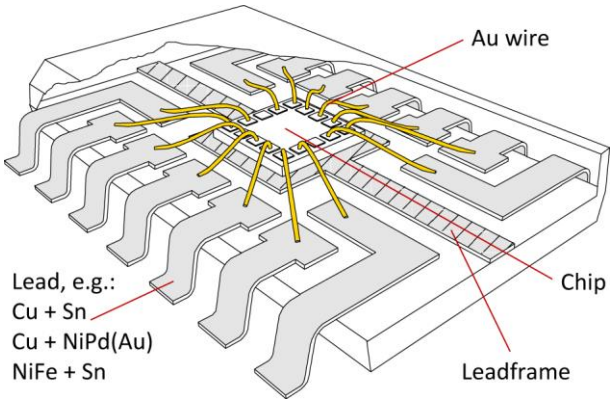

*** Insert Figure 1.5 ***

Caption: 1.5. Schematic of a small outline (SO-type) integrated circuit

Credit: [1.2]

The difference between them is that QFP packages have gull-wing-shaped lead (Fig. 1.6), while the leads of PLCC packages are bent back in 'J' shape. Similarly to these package types, the QFN (quad flat no-lead) packages do not have leads, but terminals in the form of solderable metallization on the four sides of the package.

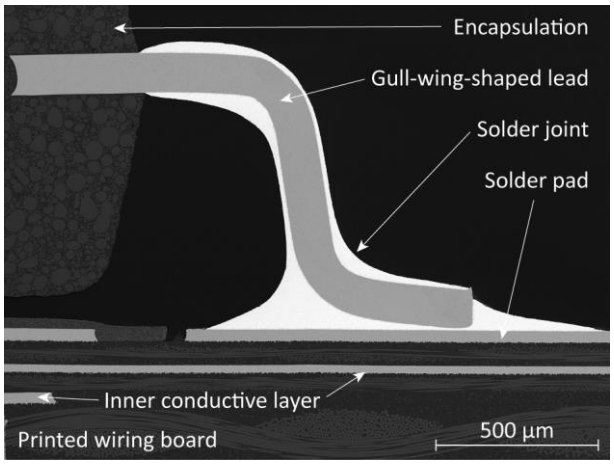

*** Insert Figure 1.6 ***

Caption: 1.6. Scanning electron microscopy image of a gull-wing shaped lead in a QFP package

Credit: –

In surface-mounted components, the lead arrangement of grid array style materializes in BGA (ball grid array) and LGA (land grid array) packages. The leads of BGA type packages have a ball shape (Fig. 1.7 – "Bump"), whereas there are no leads in LGA type packages, but metalized terminals on the bottom side of the package.

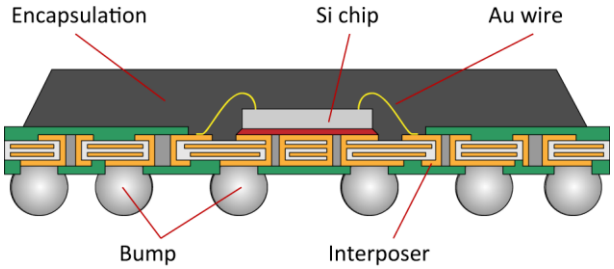

*** Insert Figure 1.7 ***

Caption: 1.7. Schematic of a ball grid array package

Credit: [1.2]

The small size, surface-mounted integrated package types are stored in plastic tapes or plastic sticks. The QFP, PLCC, QFN, BGA, and LGA type packages are stored in plastic trays for the automatic placement of the components.

The surface-mount technology has many advantages over the through-hole technology. The size of the surface-mounted components is smaller than that of the through-hole ones while having the same function. Therefore, higher integration, more functions per area unit can be achieved, resulting in smaller parasitic effects on the interconnection lines (e.g., leads, traces on the PWB) and in higher operating frequencies. Furthermore, the surface-mounted components are almost entirely standardized allowing the easy automation of component placement by placement machines.

[1.2 Reflow soldering technology]

Reflow soldering technology is the most popular and generally applied method for fastening electronic components mechanically to the PWB and connecting them electrically to the electronic circuit [1.3]. The solder material for this technology is the so-called solder paste, which is a dense suspension of solder particles and flux. The flux is responsible for the cleaning, removing oxides and contaminants from the metalized terminals to be soldered. The solder particles are made from solder alloys by ultrasonic or centrifugal atomization with a diameter of a couple of micrometers (~5–45 μm depending on the Type of solder paste) [1.4]. The solder alloys were mostly lead-bearing till the beginning of the 2000s; e.g., the eutectic tin-lead, Sn63/Pb37 alloy with a melting point of 183 °C was especially popular. Since the restriction of hazardous substances in the EU (RoHS directive), the electronic industry was urged to introduce the lead-free solder alloys. Nowadays, the most commonly used, second-generation lead-free alloys are Sn-Ag-Cu (SAC) based alloys. The SAC305 (Sn/Ag3/Cu0.5) alloy with a melting point of 217–219 °C is a universal favorite.

A huge number of research works are investigating the properties of SAC alloys. Based on these works, the wetting and the mechanical behaviors of some SAC alloys are more superior compared to the traditional Sn/Pb alloys. However for certain applications, for example under extreme operation, e.g. overpressure [1.5] or mechanical vibration, the pure SAC alloys might not perform sufficiently; therefore the development of third-generation lead-free solder alloys, even doped with microalloys (additives with less than 0.2 wt.%), or with nanoparticles is still a current topic. Some common alloys and their melting- and solidification temperatures are listed in Table. 1.2.

*** Insert Table 1.2 ***

Caption: 1.2. Solder alloys commonly used in electronics technology (composition is in wt%)

Credit: –

Solder alloy	**Liquidus point [°C]**	**Solidus point [°C]**
Sn63/Pb37	183	
Sn60/Pb40	183	188
Sn60/Pb38/Ag2	176	189
Sn95.5/Ag3.8/Cu0.7	217	218
Sn96.5/Ag3/Cu0.5	217	220
Sn98.4/Ag0.8/Cu0.7/Bi0.1	217	225
Sn98.9/Ag0.3/Cu0.7/Bi0.1	217	228
Sn91/Ag3.8/Cu0.7/Bi3/Sb1.5/Ni0.15	206	218
Sn42/Bi58	139	141

In this chapter, the elementary steps of reflow soldering technology will be overviewed. The rheological properties of the solder paste, which is one of the essential materials in this technology, will be detailed. Finally, a new measurement method will be presented for addressing not just the rheological properties but also the thixotropic behavior of solder pastes.

[1.2.1 Overview of the reflow soldering technology steps]

The reflow soldering technology consists of three basic steps. Firstly, the solder paste is deposited onto the pads of the printed wiring board by stencil printing technology. A squeegee is moved with a predefined velocity and force over the stencil and pushes the solder paste into the apertures (Fig. 1.8). After separating the printed wiring board from the stencil, the solder paste remains on the solder pads.

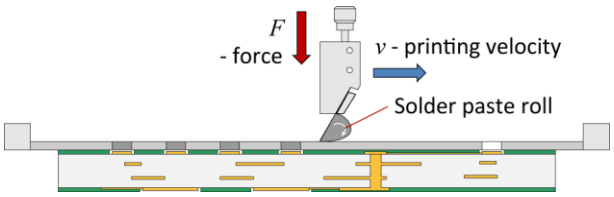

*** Insert Figure 1.8 ***

Caption: 1.8. Schematic of stencil printing

Credit: [1.6]

Next, the components are placed into the deposited solder paste by automatic placement machines. The machines pick up the component from the storage (e.g., paper tapes, plastic trays) with a vacuum nozzle, measure its location and orientation on the nozzle, and place the component by automatically adjusting positional and rotational offsets according to the prior measurements (Fig. 1.9).

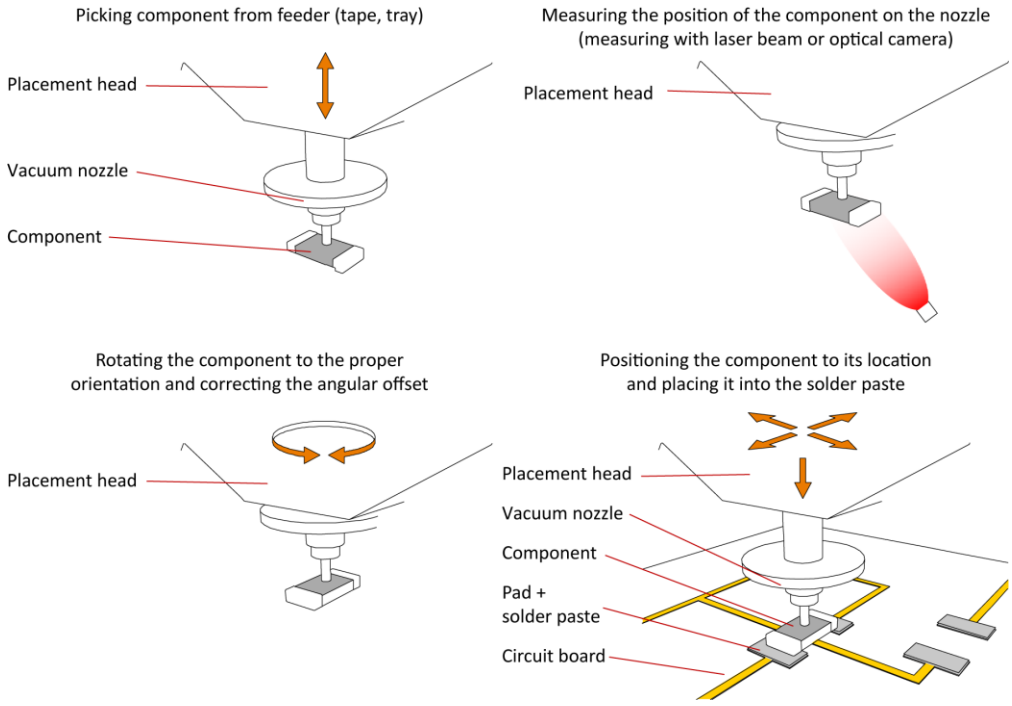

*** Insert Figure 1.9 ***

Caption: 1.9. Steps of automatic component placement

Credit: [1.2]

Two types of placement machines are distinguished from the placement head point of view: pick&place and collect&place heads. The pick&place heads pick up one component and then place it to the respective location. Contrary, collect&place heads pick up, collect several components (4, 8–32), and then place them onto the particular locations. The collect&place machines are faster than pick&place machines. The placement speed can reach several ten-thousand components per hour, but the positional error, offset is also larger (up to 20–40 μm) in the case of collect&place machines.

Lastly, the assembly travels through an oven, where the solder alloy in the solder paste is remelted, reflowed employing infrared radiation (Chapter 2), forced convection (Chapter 3), or by a phase-changing material in vapor phase soldering (Chapter 4). The molten, liquid state solder wets the metalized terminals and forms the solder joints (fillet shape). After the solder melting, the assembly cools down, the solder solidifies and establishes the mechanical and electrical connection between the components and the printed wiring board. From the quality and reliability point of views, the most important factors are the rheological properties of the solder paste [1.7], the process of stencil printing [1.8], and the physical processes take place during the reflow phase of the soldering when the solder alloy is in molten form.

[1.2.2 Rheology of solder pastes]

The solder pastes are dense suspensions of solder particles and flux, as aforementioned. The typical solid content is 50% vol% and 85–90% wt%. The particle sizes in the solder pastes vary according to the Type of the paste as defined by the IPC J-STD-005 standard [1.9] (Table 1.3).

*** Insert Table 1.3 ***

Caption: 1.3. Particle sizes in solder pastes

Credit: [1.9]

Solder paste	None larger than [µm]	Less than 1% larger than [µm]	Minimum 80% between [µm]	Maximum 10% less than [µm]
Type-1	160	150	150–75	20
Type-2	80	75	75–45	20
Type-3	50	45	45–25	20
Type-4	40	38	38–20	20
Type-5	30	25	25–15	15
Type-6	20	15	15–5	5

The generally known law describes the viscosity of Newtonian fluids, presented in (1.1) [1.10].

$$\tau = \mu \frac{\partial u}{\partial y} \tag{1.1}$$

where τ [Pa] is the shear stress, $\partial u/\partial y$ [s^{-1}] is the rate of shear, and the proportionality factor μ is the viscosity [Pa·s]. The solder pastes exhibit non-Newtonian fluid properties (1.2); the apparent viscosity of solder pastes decreases with the rate of shear ($0 \leq n \leq 1$ in expression 1.2).

$$\tau = \mu \left(\frac{\partial u}{\partial y} \right)^n \tag{1.2}$$

The rheological properties, the apparent viscosity of solder pastes are usually measured by a rotational rheometer in a plate-plate arrangement (Fig. 1.10).

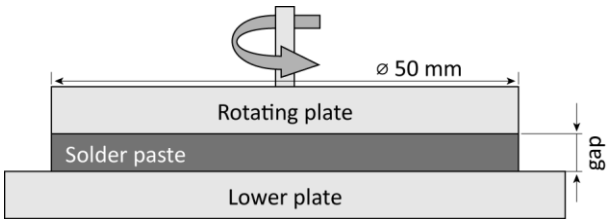

*** Insert Figure 1.10 ***

Caption: 1.10. Schematic of the rheological measurement with a rotational rheometer

Credit: [1.11]

The solder paste is placed between the upper, rotating plate, and the lower, Peltier temperature controlled standing plate. Serrated plates (e.g., with *Ra*: 4–7 µm) can be used with the view to reduce the wall-slip effect [1.12]. A hood is also used to enhance temperature control and avoid evaporation of the flux. The distance between the plates should be chosen according to the particle size in the paste. As recommended by Barnes [1.13], the gap to particle size ratio should be at least ten, i.e., 500 µm for Type-3 solder paste and 400 µm for Type-4 solder pastes as examples. After setting the measuring gap, the rotation or oscillation of the upper plate is started. The instrument controls the strain and the strain rate (strain-controlled method) and records the torque needed for the movement as a function of time. By using the geometric parameters of the measuring system, viscosity and dynamic moduli are calculated by the software of the instrument for rotational and oscillatory mode, respectively.

Many research works investigated the rheological properties of the solder pastes. Pietriková et al. [1.14] and Nguty et al. [1.15] investigated the viscosity of solder pastes by sweeping the rate of shear during the measurements, in order to present the non-Newtonian, shear-thinning properties of the pastes. They found that the apparent viscosity of solder pastes can decrease three to four orders of magnitude over the rate of

shear from 10^{-3} to 10^{2} s^{-1}. Durairaj et al. [1.16] characterized the viscosity of solder paste for future modeling of the stencil printing process with numerical methods. Glinski et al. [1.17] suggested implementing non-Newtonian viscosity parameters in the numerical modeling of stencil printing instead of using Newtonian fluid properties. Durairaj et al. [1.18] highlighted the differences between the two approaches (Newtonian or non-Newtonian fluid properties) with calculations for different printing speeds. They suggested using the Cross material model (1.3) [1.10] for describing the viscosity decrease with an increasing rate of shear.

$$\eta_{Cross} = \eta_{\infty} + \frac{\eta_0 - \eta_{\infty}}{1 + \left(\lambda \dot{\gamma}\right)^n} \tag{1.3}$$

where η_0 is the zero-shear viscosity, η_{∞} is the infinite-shear viscosity, λ is the time constant, $\dot{\gamma}$ is the rate of shear, and n is a power-law index.

However, Al-Ma'aiteh et al. [1.19] found that the viscosity curve of solder pastes has a plateau region at low rates of shear, approximately from 10^{-3} to 10^{-2} s^{-1} in their work (Fig. 11). This nature of the viscosity curve can be captured with the Carreau-Yasuda material model (1.4) [1.20].

$$\eta_{C-Y} = \eta_{\infty} + \frac{\eta_0 - \eta_{\infty}}{\left[1 + \left(\lambda \dot{\gamma}\right)^a\right]^{\frac{1-n}{a}}} \tag{1.4}$$

where a is the Yasuda exponent.

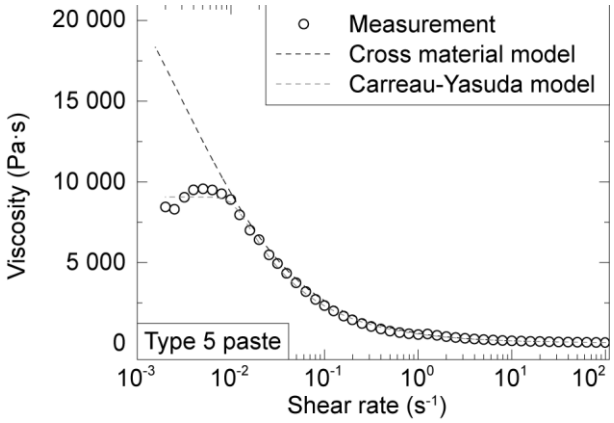

*** Insert Figure 1.11 ***

Caption: 1.11. Viscosity curve of a Type-5 solder paste

Credit: –

Goodwin [1.21] showed that the rheological parameters did not depend on the size distribution of metal particles in the paste, but on their volume fraction. He presented that the effect becomes apparent at volume fractions higher than 30% vol%. Solder pastes usually have 50% vol% of metal particles in the total volume, so Goodwin's results suggest that the viscosity does not depend on the particle size. Nevertheless, according to empirical and industrial experiences, solder pastes exhibit thixotropic behavior (time-dependent shear thinning) on the one hand, and their viscosity depends on the particle size on the other hand. Goodwin et al. could not show this phenomenon possibly because they measured suspensions only in their initial state, and the thixotropic behavior was not considered.

Dynamic, time-dependent characteristics were also investigated in the literature. Nevertheless, only constant rates of shear were applied in the measurements for revealing the viscosity change over time, and the lowest rates of shear were relatively high, from 0.1 [1.22] to 2 s^{-1} [1.23]. These works also did not take into account the thixotropic

behavior of solder pastes and the idle time between individual stencil printings, which is generally between 15 s and 60 s [1.24]. One particular research dealt with the thixotropic behavior where a sequence of measurements was used for addressing this property of solder pastes [1.12]. However, only a narrow shear rate sweep (from 0.01 to 0.2 s^{-1}) was applied and no idle time between the measurements was set. The effect of idle time was investigated based on structure kinetics in the work of Vachaparambil et al. [1.25], but only a longer duration of idle-time (~100 s) was used, which is not common in stencil printing.

These shortcomings were addressed by the research wok of Krammer et al. recently [1.11]. They focused on improving the characterization of viscosity for enhanced numerical modeling of the stencil-printing and better process optimization. Three solder pastes (Type 3, Type 4, and Type 5) were investigated and compared in that work. Special attention was paid on the choice of identical flux for all tested pastes so that the flux did not alter the results. The rate of shear varied from $1.5 \cdot 10^{-4}$ to 10^{2} s^{-1} within their measurement. The idle time of stencil printing was addressed by letting the samples rest for a given time frame between individual measurement cycles. This "rest-period" was matched with the idle time of stencil printing since its length affects the thixotropic behavior of solder pastes significantly. Therefore, the samples were allowed to rest in the experiment for 15, 30, 60 s (length of 'b' in Fig. 12), and eight measurement series were carried out automatically in all of the cases. The schematic of the test run (rate of shear over time) and the theoretical change in viscosity are illustrated in Fig. 12.

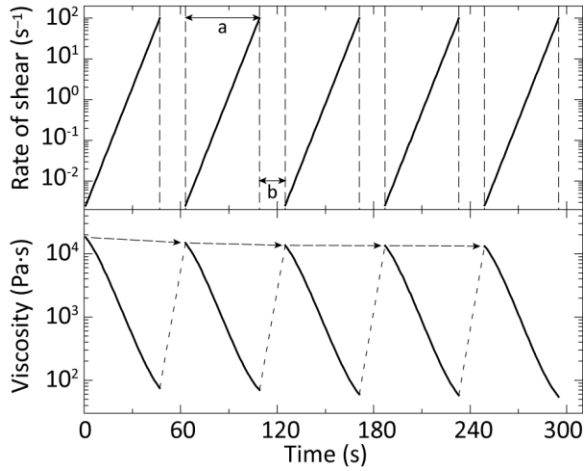

*** Insert Figure 1.12 ***

Caption: 1.12. Viscosity curve of a Type-5 solder paste

Credit: [1.11]

Krammer [1.11], Pabst [1.27], and also Zhang [1.28] found that no difference in viscosity can be shown between the different types of solder pastes in the initial state, after the first measurement cycle. The difference in the viscosities between the solder pastes was below 10% (Fig. 1.13), which is in the order of magnitude of the measurement uncertainties.

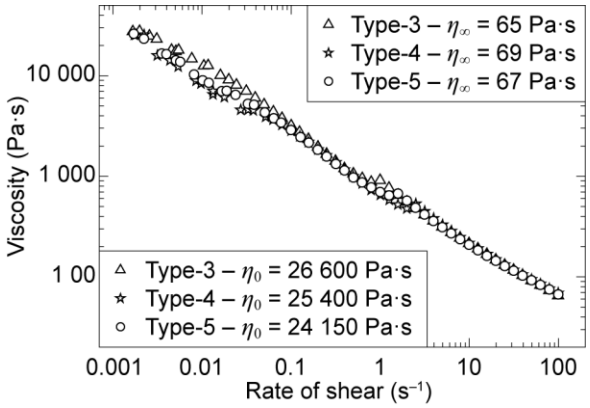

*** Insert Figure 1.13 ***

Caption: 1.13. The viscosity curves of solder pastes in the initial state

Credit: [1.11]

Contrary to these findings, Krammer et al. [1.11] showed that there is a significant decrease in the viscosity of solder pastes over the measurement cycles on the one hand (Fig. 1.14).

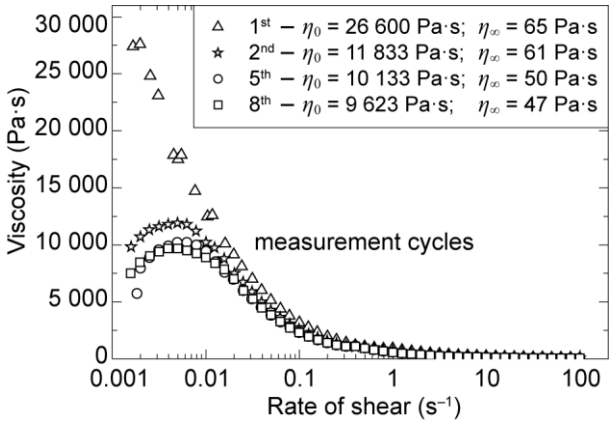

*** Insert Figure 1.14 ***

Caption: 1.14. The viscosity curve of a Type-3solder paste over the measurement cycles

Credit: [1.11]

On the other hand, noteworthy differences can be shown in the zero-shear and infinite-shear viscosity values between the different types of solder pastes in the stabilized state, i.e., after eight measurement cycles. The difference in zero-shear viscosity could even be 30% (Fig. 1.15), whereas the infinite-shear viscosity can vary for the different solder pastes by 20–30% (Fig. 1.16). These differences imply that for the numerical modeling of stencil printing, that viscosity curve of solder pastes should be utilized, which were measured in their stabilized state.

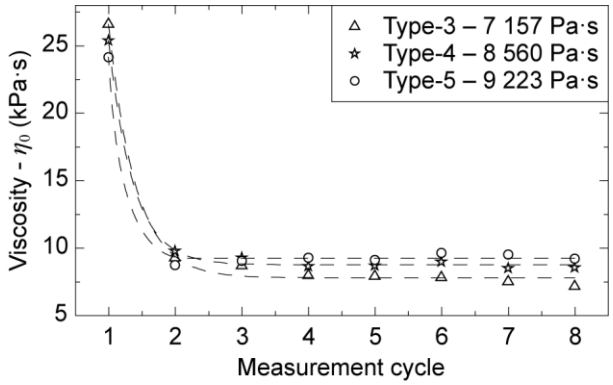

*** Insert Figure 1.15 ***

Caption: 1.15. Zero-shear viscosities of solder pastes in their stabilized state

Credit: [1.11]

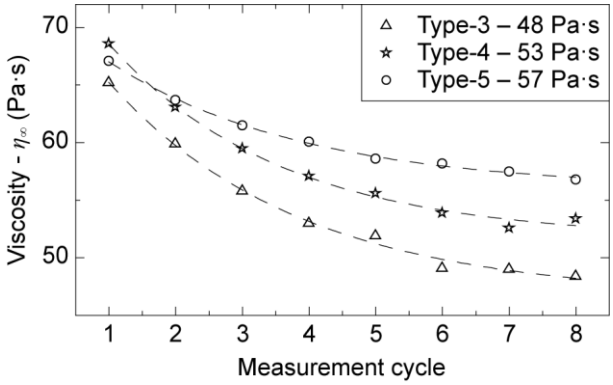

*** Insert Figure 1.16 ***

Caption: 1.16. Infinite-shear viscosities of solder pastes in their stabilized state

Credit: [1.11]

Oscillatory stress sweep tests were also performed in the research work of [1.11] in the stabilized state (after eight measurement cycles) of the solder pastes. An important parameter of the oscillatory measurement results is the so-called cross-over stress, where the values of storage (G′) and loss modulus (G″) are equal to each other. Bao et al. demonstrated that the lower the stress at G′ = G″, the more liquid-like the solder paste is, which could result in paste fracture in stencil printing during the stencil separation

process [1.29]. Furthermore, slump defects after the printing can occur more frequently with solder pastes exhibiting lower values of cross-over stress. Krammer et al. presented in [1.11] that their Type-3 solder paste showed significantly lower cross-over stress compared to that presented by the Type-5 solder paste (Fig. 1.17). This result also proved that more precisely defined deposits in stencil printing can be achieved by using solder pastes with smaller particle sizes.

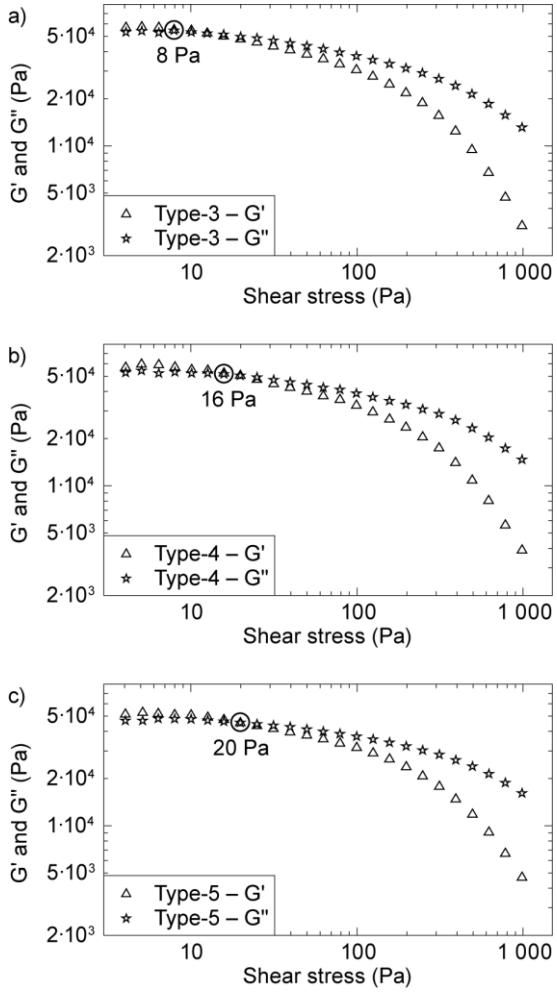

*** Insert Figure 1.17 ***

Caption: 1.17. Oscillatory stress sweep test: a) solder paste Type-3; b) solder paste Type-4; c) solder paste Type-5

Credit: [1.11]

[1.3 Stencil printing]

Stencil printing might be the most crucial step in reflow soldering technology. Even 60–70% of the soldering failures can be traced back to this process; principally the formation of solder bridges and open joints. In this chapter, the process of stencil printing will be discussed both from the process parameters and from the related assembly defects point of view. Structure of traditional stencils and the so-called Vectorguard frame system will be given. The numerical modeling aspects of the stencil printing process will be discussed. Detailed description about the modelling of reflow ovens is presented in Chapter 6. This subchapter is confined exclusively to present some modelling aspects only in connection with the process of stencil printing.

[1.3.1 The process of stencil printing]

As mentioned above, the process of stencil printing is responsible for providing the solder paste onto the soldering pads by a fast, mass deposition process. The process of stencil printing can be divided into three sub-steps. At first, the stencil, which is a 50–200 μm thick metal foil, is perfectly aligned to the printed wiring board. The apertures in the stencil are formed according to the solder pads on the substrate. Next, the solder paste is forced into the apertures by a squeegee stroke with predefined pressure and velocity. Lastly, the printed wiring board is separated from the stencil with a predefined speed (6–8 mm/s); the solder paste is released from the apertures and remains on the solder pads (Fig. 1.18).

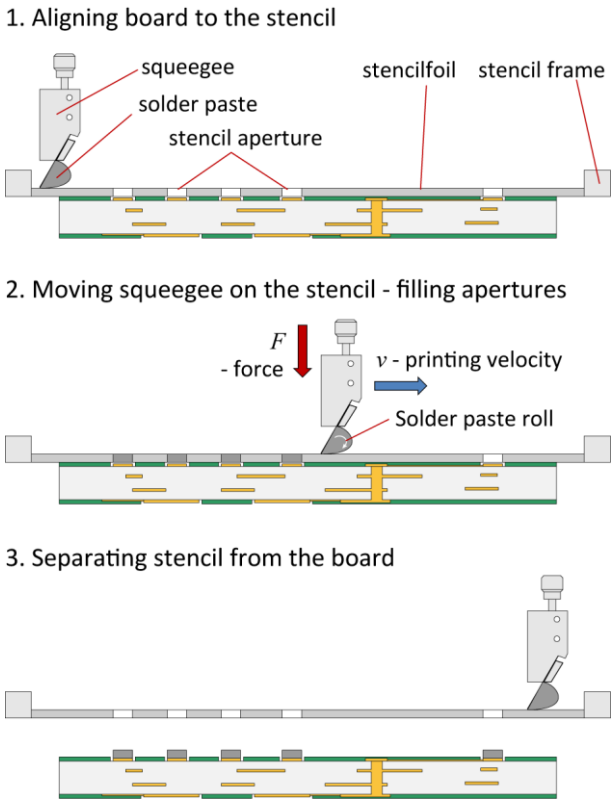

*** Insert Figure 1.18 ***

Caption: 1.18. The sub-steps of stencil printing

Credit: [1.2]

The stencil, which is a key tool in stencil printing, is usually made from stainless steel or nickel. Its thickness ranges typically from 50 to 200 µm. The apertures (openings) are designed precisely according to the soldering pads on the printed wiring board. There are three techniques for forming the apertures within the stencil, namely: chemical etching, laser cutting, and electroforming. All of them have advantages and disadvantages. Chemical etching is the cheapest method, the price of the stencil depends on the foil size, but it provides the worst quality stencils, which are appropriate for pitch sizes above 0.63 mm. Laser cutting is the most widespread technique for preparing stencils. Their price is moderate depending on the number of apertures, and they are

appropriate for pitch sizes down to 0.4 mm and for passive discrete components down the size code of 0201. Both of these technologies are subtractive ones; the preparation of the stencil is started from a full sheet of foil and, the material is removed from the places where apertures should be formed. The best quality stencils can be prepared by electroforming for a relatively high price. They are perfect for ultra-fine pitch integrated circuit packages and the smallest passives. The price of electroformed stencils depends on the thickness of the foil, but note that the fine-pitch components require thinner stencils (approx. 50–75 μm). The traditional structure of stencils as a tool is illustrated in Fig. 1.19. It is consisting of the stencil foil itself, an aluminum frame for handling, and a metal mesh for tensioning the foil by approximately 50 N/cm. As aforementioned, the layout of the apertures is designed appropriately to soldering pads. Furthermore, alignment marks (fiducial points) are engraved on the bottom side of the stencil for aiding its positioning to the printed wiring board. The fiducial points are filled with black epoxy yielding better contrast by the automatic optical inspection of them.

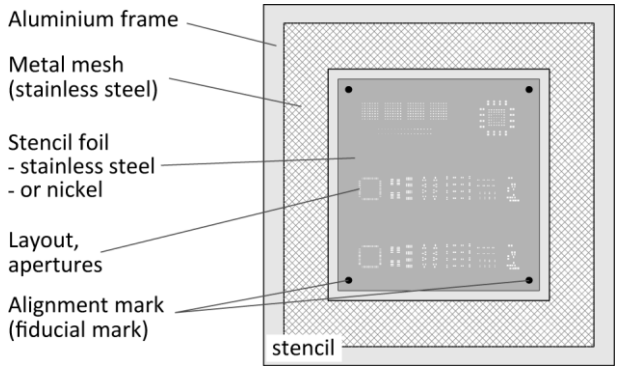

*** Insert Figure 1.19 ***

Caption: 1.19. Structure of a traditional stencil

Credit: [1.2]

Besides the traditional stencils, the so-called Vectorguard stencils (stencil frames) are also used. In this stencil frame, the foils are interchangeable. During operation, springs tighten aluminum profiles, which cling into the grooves formed along the edges of the stencil foil. Ahead of the springs, there is a silicone tube. By blowing up the tube with compressed air, the profiles open, and the stencil foil can be inserted into the frame. By deflating the tube, the profiles close and the stencil foil becomes tight (Fig. 1.20). The advantage of this system is that the stencil itself can be thinner allowing easier transport and storage. Slight disadvantage by industrial experiences is the somewhat lower reliability of the tensioning system.

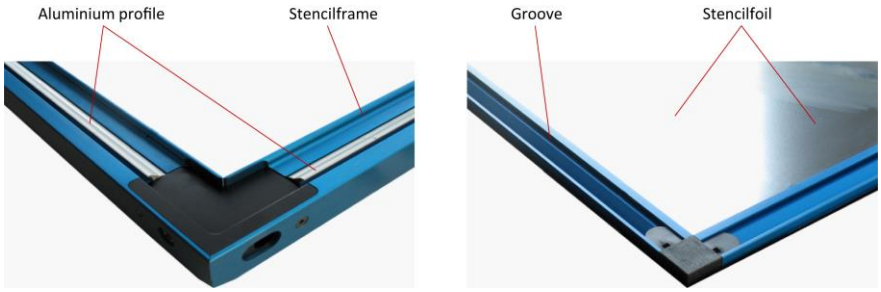

*** Insert Figure 1.20 ***

Caption: 1.20. Vectorguard stencil frame

Credit: –

[1.3.2 Process parameters and related printing failures]

The main process parameters of stencil printing include the printing speed (velocity of stroke), specific printing force, attack angle of the squeegee, stencil separation speed, intervals between stencil cleaning, and ambient conditions in the printer. The main characteristic of the stencil printing process is the so-called transfer efficiency (1.5), which is the ratio of the deposited solder paste volume to the volume of stencil aperture.

Deviance of ±25% is allowed usually in the industry for this parameter. The transfer efficiency depends not only on the process parameters but on the manufacturing technology of the stencil and on the size of stencil aperture as well. The size of the stencil aperture is usually characterized by two ratios, by the aspect ratio (AS) and the area ratio AR, which is the ratio of the stencil aperture area to the wall surface of the stencil aperture (1.6). For expecting a transfer efficiency over 75%, the aspect ratio should be larger than 1.5, and the area ratio should be larger than 0.66 by empirical findings for each and every aperture in the stencil.

$$TE = \frac{V_{paste}}{V_{aperture}} \tag{1.5}$$

$$AS = \frac{w}{t} \geq 1.5; \quad AR = \frac{w \cdot l}{2(w+l)t} \geq 0.66 \tag{1.6}$$

where *w* and *l* are the shorter and longer sides of a rectangular aperture, respectively, and *t* is the thickness of stencil foil. Typically the rule regarding area ratio is used for determining the proper foil thickness for a given assembly, by analyzing its value for critical apertures (mostly at fine-pitch components), and ensuring that to be larger than 0.66 by reducing the foil thickness. A theoretical curve of transfer efficiency (as a function of area ratio) fitted to a measurement of a Type-3 solder paste is illustrated in Fig. 1.21.

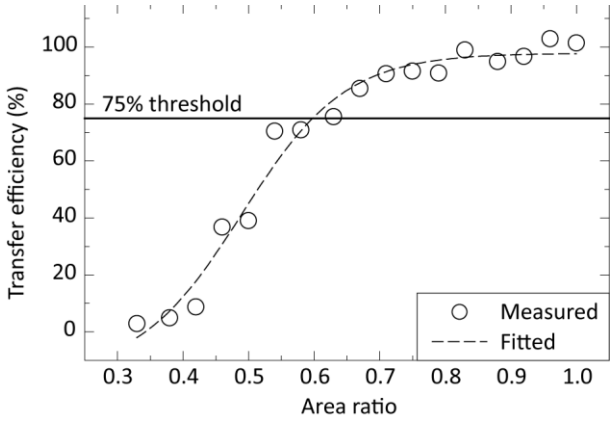

*** Insert Figure 1.21 ***

Caption: 1.21. Transfer efficiency over the area ratio of stencil apertures

Credit: –

The printing speed is usually can be set between 10 and 300 mm/s in stencil printers, but typical values are from 30 to 70 mm/s. If the printing speed is set to a too high value, rolling of the solder paste ahead of the squeegee can cease, and aperture skipping (no solder paste is deposited into) might occur, resulting in open joints after soldering. Too slow printing speed does not affect the printing quality significantly but reduces the throughput of the process itself.

The usual value for the specific printing force is 0.3 N/mm. It should be noted that giving the value of the printing force instead of the specific force (e.g., in datasheets) can be misleading, since there are several lengths of squeegees (20, 30, 40 mm), which are used in the industry for stencil printing. By the optimization of this parameter, the value of the specific printing force can be reduced until the value, when the stencil is completely wiped during the stroke, and its surface is free from solder paste residues. Since the pressure over a stencil and similarly over a squeegee due to the roll of solder paste depends on the printing speed (see Chapter 1.3.3), lower specific printing force can

be enough for lower printing speeds, and larger force values are optimal for faster strokes. If the printing force is too large, the squeegee and the stencil can wear out rapidly. If the printing force is too low, a layer of solder paste is left on the surface of the stencil after printing (Fig. 1.22), which can result in higher solder paste deposits on the printed wiring board than the thickness of the stencil, yielding solder bridges after soldering. It should be noted that in industrial stencil printers, there are two squeegees, one for the forward direction for printing the n^{th} assembly and one for the backward direction for printing the $n + 1$ assembly.

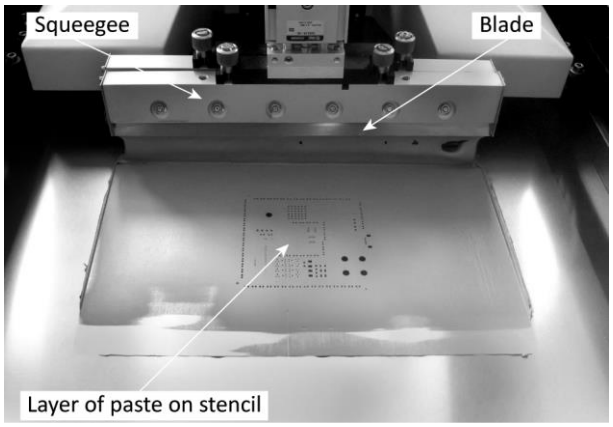

*** Insert Figure 1.22 ***

Caption: 1.22. A layer of paste remains on the stencil because of too low printing force

Credit: –

The stencil separation speed can be set approximately between 1 mm/s and 10 mm/s. The rheological properties of today solder pastes are designed for allowing faster stencil separation speeds like 6–8 mm/s. If the separation speed is set to a too low value, edge of the solder paste deposit can be lifted (“dog-ears” effect) while separating the printed wiring board from the stencil, resulting in an uneven deposit surface and height (Fig. 1.22). If the stencil separation speed is set to a too high value, the viscosity of the

deposited solder paste can also remain high (thixotropic behavior). As a consequence, the deposited solder paste cannot keep its shape; it can slump and can form bridges between adjacent component leads.

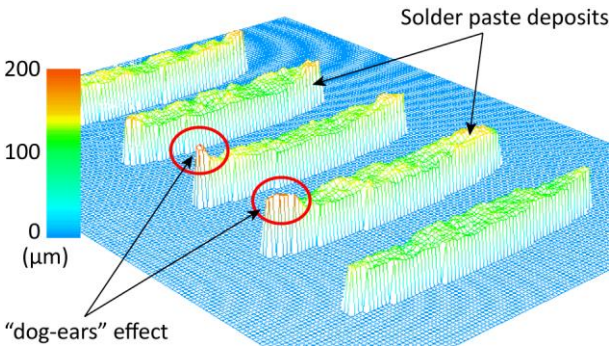

*** Insert Figure 1.23 ***

Caption: 1.23. SPI (solder paste inspection) image of deposits for QFP component; edge of solder paste is lifted ("dog-ears") because of inappropriate stencil separation speed

Credit: –

The automatic cleaning interval of the stencil is also an essential parameter. During the printings, the solder paste sticks in a given extent to the walls of the stencil aperture, and a layer of solder paste continuously build up there, resulting in lower transfer efficiency. In the end, the solder paste can completely block the aperture, yielding open joints after soldering. Cleaning of the stencil can be performed by a dry cloth, by a wet cloth (impregnated by the solvent of solder paste) and by those together with vacuum aiding. The stencil is cleaned automatically within around 5–10 printings, and the optimal interval is usually determined with an experiment, where the transfer efficiency is measured over the printings without stencil cleaning. A typical result of this experiment is illustrated in Fig. 1.24.

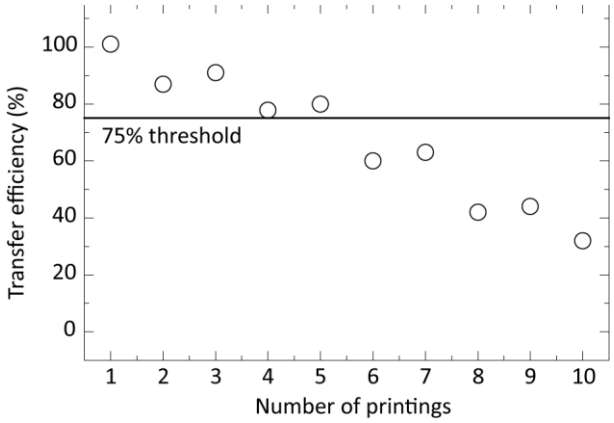

*** Insert Figure 1.24 ***

Caption: 1.24. Transfer efficiency over the number of printings without stencil cleaning

Credit: –

The recommended interval between stencil cleanings is the number where the transfer efficiency decreases below 75%. A slight oscillation can be observed in the results between the onward and backward traveling squeegees if the given stencil printer lacks a closed-loop squeegee force control system. In newer systems, the stencil cleaning interval can be optimized continuously over time by the machine-to-machine communication between the stencil printer and the SPI (solder paste inspection), in the concept of Industry 4.0.

Last but not least, the support system of printed wiring boards also affects the quality of stencil printing. In modern stencil printers, either the support pins are placed automatically by the printer, or the support system itself includes pneumatically-operated pins that automatically adapt to the board surface (note that there are components on the bottom side in double-sided assemblies). Nevertheless, if the support pins are set inappropriately, the solder paste can remain on the surface of the stencil (Fig. 1.25) at specific locations (where the PWB can bend away from the stencil), indicating that the

deposited solder paste will be too high on the printed wiring board according to those places on the stencil. Furthermore, the solder paste can dry onto the bottom surface of the stencil ("bleeding of the solder paste between the stencil and board"). Considering the particle size of approximately 40 µm and the stencil thickness of approximately 120 µm, "bleeding" can cause even a 30% increase in the deposited volume of solder paste. Both printing defects can results in solder bridges after the soldering.

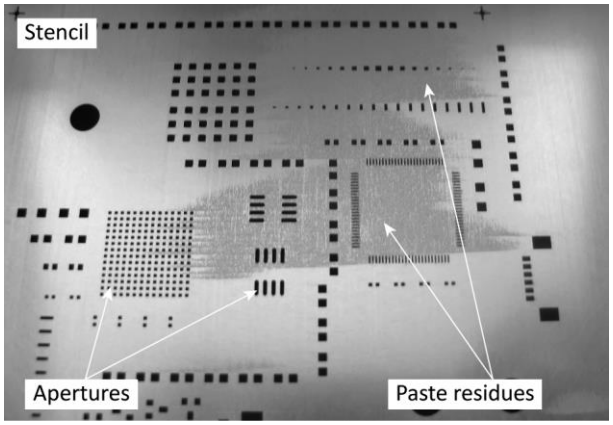

*** Insert Figure 1.25 ***

Caption: 1.25. Solder paste residues on the surface of the stencil because of inappropriate support

Credit: –

[1.3.3 Numerical modelling of stencil printing]

Since stencil printing is considered to be the critical step in eliminating soldering failures – ~60% of soldering failures can be traced back to this process [1.8] –, exhaustive optimizations of the process are continuously carried out using numerical modeling, and recently even utilizing methods based on machine learning. The flow of

the solder paste can be described by beginning with the Navier-Stokes equation (1.7) [1.30]:

$$-\frac{1}{\rho}\nabla p = \frac{\partial \mathbf{u}}{\partial t} + \mathbf{u}\cdot\nabla\mathbf{u} - \frac{\mu}{\rho}\nabla^2\mathbf{u} - \mathbf{f} \tag{1.7}$$

where ρ is the density of the fluid, p is the pressure, $\mathbf{u}$ is the flow velocity, μ is the dynamic viscosity, and $\mathbf{f}$ represents body accelerations acting on the continuum. The solder paste can be considered as an incompressible fluid (ρ is constant). Hence the equation of mass continuity reduces to the equation of volume continuity (1.8) [1.31]:

$$\nabla\cdot\mathbf{u} = 0 \tag{1.8}$$

In the case of stencil printing, the flow velocity is relatively low, and the viscosity of solder pastes is relatively high. The term of the convective acceleration ($\mathbf{u}\cdot\nabla\mathbf{u}$) is insignificant compared to the term of diffusion ($\mu\cdot\rho^{-1}\nabla^2\mathbf{u}$) in the Navier-Stokes equation (1.7). Furthermore, the Reynolds number (1.9) is much lower than 1 ($\mathrm{Re} < 10^{-2}$ based on the work of Durairaj et al. [1.18]), which implies a laminar flow.

$$\mathrm{Re} = \frac{\rho\cdot u\cdot L}{\mu} \tag{1.9}$$

where u is the magnitude of the flow velocity, and L is the characteristic length. As a consequence, the flow field of the solder paste can be described by the Stokes flow (1.10) in steady-state, as shown by Constantinscu [1.32]:

$$\nabla p = \mu\nabla^2\mathbf{u} + \mathbf{f} \tag{1.10}$$

where $\mathbf{f} = 0$ in this case.

The finite volume method (FVM) is used typically for approximating the fluid flow equations numerically. Furthermore, the solder paste is usually considered as a homogenous liquid, utilizing single-phase calculations. The geometry of the model

usually consists of the stencil and the squeegee as solid walls and the solder paste as the fluid. The system is generally represented in an opposite frame of reference, which means that the squeegee is a static wall, whereas the stencil moves by the printing speed in the opposite direction to the printing. Both the stencil and the squeegee have a no-slip boundary condition, meaning that the velocity of the first fluid layer next to the respective wall is equal to the velocity of that wall. The remaining fluid interface (paste-air interface) has a free-slip boundary condition, meaning that the tangential velocity of the first fluid layer and the shear stress along the interface is zero. Finally, the system can be modeled to be isothermal (1.11), since Mannan et al. [1.33] have found that the heat generated inside the solder paste roll during the printing is conducted away so that temperature does not rise noticeably.

$$\mathrm{d}T/\mathrm{d}t = 0 \tag{1.11}$$

where T is the absolute temperature. The geometry with the various boundary conditions is illustrated in Fig. 1.26.

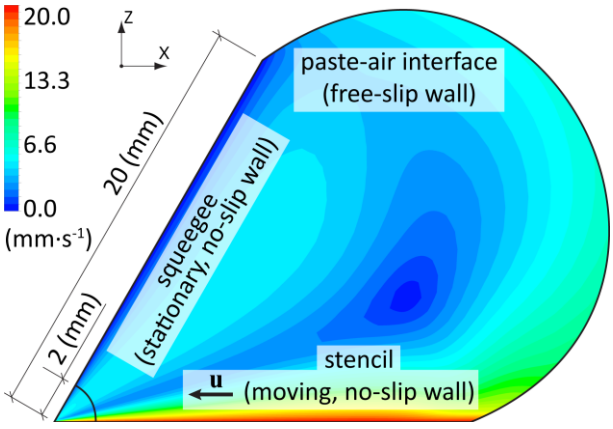

*** Insert Figure 1.26 ***

Caption: 1.26. Finite volume model of stencil printing

Credit: [1.6]

The material property for the fluid should be set to describe the non-Newtonian behavior of the solder paste, using either the Cross or the Carreau-Yasuda model (see Chapter 1.2.2). Many researchers proposed using the Cross material model to define the apparent viscosity over the rate of shear. However, Krammer et al. [1.11] showed that there is a plateau range in the viscosity curve of pastes at low rates of shear (from 10^{-2} to 10^{-3} s^{-1}). This suggests that the Carreau-Yasuda model (described by Boyd and Buick in [1.20]), which is similar to an inverted S-curve can be a better approach for determining the apparent viscosity of solder pastes.

The validation of the numerical model regarding stencil printing can be performed based on the work of Riemer. He started the numerical modelling of printing processes at the end of the ’80s by developing an analytical model (based on the Navier-Stokes equation) to predict the pressure distribution along the surface of a mask in printing processes (screen printing or stencil printing) [1.34]. He found that the pressure distribution (which is commonly used for subsequent calculations) depends on three parameters: the squeegee angle, the printing velocity, and the viscosity of the solder paste (1.12) [1.35]. These parameters are the most significant, which are affecting the aperture filling of solder pastes, or paste release during stencil separation.

$$P = \frac{1}{r}\left(\frac{2\sin^2\theta}{\theta^2 - \sin^2\theta}\right)\mu \cdot u \tag{1.12}$$

where P is the pressure at a distance r from the squeegee (x-direction in Fig. 1.26 at $z = 0$), θ is the attack angle of the squeegee, μ is the dynamic viscosity, and u is the printing velocity. The pressure depends on the velocity and on the viscosity linearly. Note that Riemer solved the Navier-Stokes equation considering Newtonian fluid properties,

so the validation of the numerical model regarding stencil printing should begin with setting Newtonian properties to the solder paste, e.g., a viscosity of 200 Pa·s.

The pressure during printing depends on the squeegee angle by a decaying exponential function (Fig. 1.27), resulting in that the squeegee attack angle (45° or 60° in the unloaded state) has a major influence on the results of stencil printing, especially in pin-in-paste technology (Chapter 1.6). The pressure along the surface of the stencil is two times higher for squeegees with a 45° angle than those with a 60° attack angle during the printing.

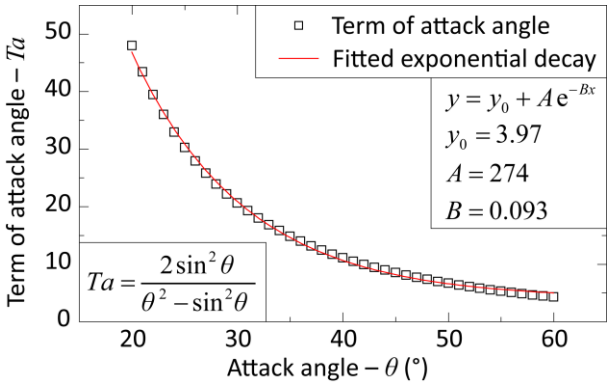

*** Insert Figure 1.27 ***

Caption: 1.27. Finite volume model of stencil printing

Credit: [1.6]

Both Seo et al. [1.36] and Glinski et al. [1.17] analyzed the pressure distribution along the surface of the stencil for different squeegee angles by numerical models. Though, they have applied nominal, unloaded squeegee angles, not the real attack angles. The real attack angle is always lower than the unloaded one due to the actual printing force. Krammer et al. [1.37] investigated the decrease in attack angle both empirically and utilizing a finite element method. They built custom equipment to measure the deformation of the printing squeegee. The load arm was chosen to be long enough to span

the whole width of the stencil (50 × 50 cm), and to be able to produce a load close to industrial standards (e.g., 0.3 N/mm) using precision weight calibers (approx. 500 grams each). The printing squeegee consists of two main parts, a holder to fasten the blade and the blade to transfer the paste through the stencil, as it is illustrated in Fig. 1.28. The overhang size of the blade was 15 mm, its thickness was 200 µm, and its unloaded angle was 60°.

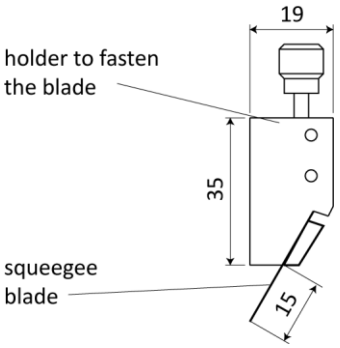

*** Insert Figure 1.28 ***

Caption: 1.28. The geometry of a squeegee tool (all dimensions are in mm)

Credit: [1.37]

With the constructed measuring equipment, different loads were applied to the squeegee tool through the measuring probe of a fixed dial indicator; and the vertical displacement of the tool was measured by the dial indicator itself. The measuring range of the indicator was 0–10 mm, while its resolution was 1 µm. The loads were applied through a loading arm (Fig. 1.29.), and the load force was varied from 22 N to 131 N.

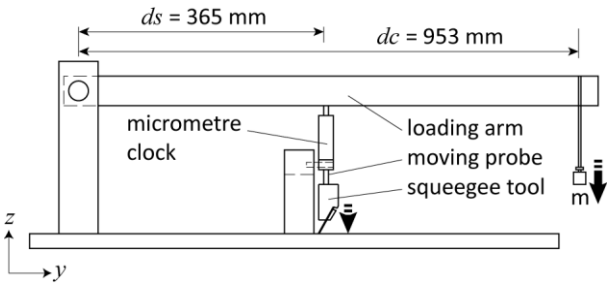

*** Insert Figure 1.29 ***

Caption: 1.29. Custom equipment for measuring squeegee deformation for different loads

Credit: [1.37]

The resolution of the load force was 1.9 mN obtained by (1.13):

$$Res = al \cdot (ds/dc) = 5 \cdot (365/953) = 1.9\,\text{mN}, \tag{1.13}$$

where *al* is the accuracy of applied load weights (5 mN), *ds* is the distance of squeegee from the lever pivot point (365 mm), and *dc* is the distance of load weights from the lever pivot point (953 mm).

After measuring the deformation of the squeegee, its FEM model was created using a 3D elastic-plastic material model of steel. The movement of this squeegee was not constrained; it was free to move, rotate, and bend in all directions. The measured and simulated results can be seen in Fig. 1.30 and simulated blade angles are indicated along the graph. It can be seen that a squeegee with these initial parameters can bend such an extent that its attack angle decreases to 53° from the initial value of 60°.

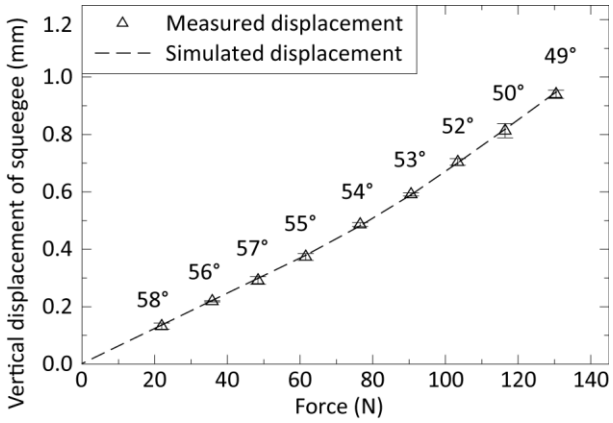

*** Insert Figure 1.30 ***

Caption: 1.30. Measured and calculated displacement of a 200 µm thick, stainless steel squeegee for various loads

Credit: [1.37]

In their next work, Krammer et al. investigated further the decrease in attack angle of squeegees, for various overhang sizes (6, 15, 20, 25 mm) and for the two initial angles of 45° and 60° [1.38]. They highlighted that in the case of large overhang sizes (e.g., 25 mm) the unloaded squeegee angles of 60° and 45° can decrease to even 42° and 21°, respectively. The changes in the attack angle for the various parameters are listed in Table 1.4.

*** Insert Table 1.4 ***

Caption: 1.4. Loaded squeegee angles for a specific printing force of 0.3 N/mm

Credit: [1.38]

Unloaded angle [°]	**Overhang sizes**			
	6 mm	**15 mm**	**20 mm**	**25 mm**
60°	58.9	53.4	48.4	42.1
45°	43.5	35.7	28.8	20.5

The expressions for the loaded squeegee angles with the mentioned conditions are given in (1.14) and (1.15) [1.38]:

$$\alpha_{a|\alpha_u=60°} = 60 - 0.026 \cdot S_O - 0.0276 \cdot S_O{}^2, \tag{1.14}$$

$$\alpha_{a|\alpha_u=45°} = 45 - 0.0789 \cdot S_O - 0.0363 \cdot S_O{}^2, \tag{1.15}$$

where α_a is the attack angle, α_u is the unloaded angle, and S_O is the overhang size.

Besides, they found that the deformation of the squeegee is quite similar along its length, denoting that a two-dimensional numerical model can be a correct approach in the investigation of stencil printing [1.38].

In the numerical modelling of stencil printing, many research works [e.g., in 1.17 and 1.36] utilized the unloaded angle of the squeegee; they analyzed the differences between the unloaded angles of 45° and 60° for example. Nevertheless, Krammer et al. showed the difference in the numerical results of these models as a function of a decrease in the squeegee attack angle [1.6]. The change in attack angle and consequently, the increase in the pressure was negligible for the loaded squeegee with an overhang size of 6 mm. Contrary, the differences were noteworthy for longer overhang sizes. In the case of the commonly used overhang size of 15 mm, the decrease in attack angle from 60° to 53.5° resulted in a pressure increment of approximately 22%. The pressure increment was even larger for longer overhang sizes; 45% and even 90% for overhang sizes of 20 and 25 mm, respectively. These changes in pressure indicated that the printing force, the geometry of the squeegee, and eventually, the resultant attack angle should absolutely be taken into account during the numerical modelling of the stencil printing process (Fig. 1.31).

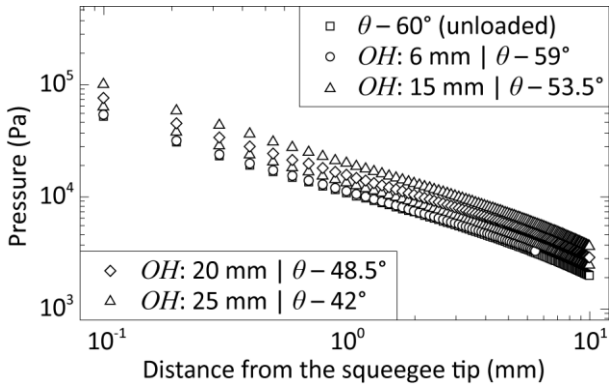

*** Insert Figure 1.31 ***

Caption: 1.31. Pressure values over the stencil (unloaded squeegee angle is 60°)

Credit: [1.6]

The changes in pressure are illustrated in Fig. 1.32 for the unloaded squeegee angle of 45°. The results were similar to the case of the unloaded squeegee angle of 60°, but the increase in pressure was even more pronounced; ~45%, ~102%, and ~250% for the overhang sizes of 15, 20, 25 mm, respectively [1.6].

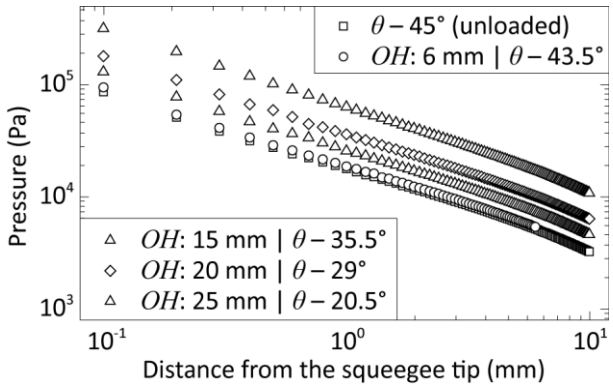

*** Insert Figure 1.32 ***

Caption: 1.32. Pressure values over the stencil (unloaded squeegee angle is 45°)

Credit: [1.6]

The exponential change in pressure over the attack angle has been presented in Fig. 1.27 for Newtonian fluid properties, and also analyzed for the non-Newtonian case. The

pressure values were evaluated at three locations: at a distance from the squeegee tip of 0.1 mm, 1 mm, and 10 mm, and illustrated in Fig. 1.33 [1.6]. The parameters of the exponential fit (collected in Table 1.5.) were also determined for these cases, and the average of the exponential decay coefficient was found to be 0.075. This value of the decay coefficient indicates even a slightly higher increase in pressure for decreasing attack angles in the case of non-Newtonian fluid properties compared to that by Newtonian fluid properties.

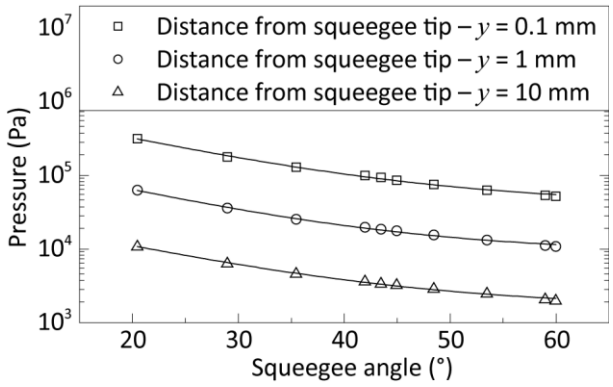

*** Insert Figure 1.33 ***

Caption: 1.33. Pressure as a function of squeegee angle (valid for the investigated fluid properties)

Credit: [1.6]

*** Insert Table 1.5 ***

Caption: 1.5. Parameters of the exponential fit to the pressure change over the squeegee angle (Fig. 1.33)

Credit: [1.6]

Parameter	**y = 0.1 mm**	**y = 1 mm**	**y = 10 mm**
y_0	40 493 Pa	9 002 Pa	1 615 Pa
A	1 248 320 Pa	260 551 Pa	40 920 Pa
B	0.074	0.077	0.073

As a summary, it was proven that neglecting the squeegee force and/or the exact geometry of the squeegee in the modelling of stencil printing, and thus utilizing inappropriate attack angle, leads to significant calculation errors. In the case of the unloaded squeegee angle of 60°, the error can reach up to 90%, whereas at the 45°

unloaded angle, the error can reach even 250%. Taking these geometrical parameters into account is therefore strongly recommended for appropriate and valid calculation results in this field. By obtaining more precise and reliable calculation results, the optimization of the stencil printing process could be more productive also for critical assembly methods, like the pin-in-paste technology (see Chapter 1.6).

[1.4 Component placement]

By the continuous decrease in the size of the surface-mounted components, the accuracy of placement machines is getting more critical, even if the surface-mounted components can self-align during the soldering (see Chapter 1.5). As mentioned in Chapter 1.2.1, two types of placement machines are distinguished from the placement head point of view; the pick&place and collect&place heads. From these, collect&place machines (which place typically passive components) are the faster but, the less accurate ones. However, the size of the passive discrete components reduced to 200 × 100 μm recently. Therefore, both the machine capability itself, and the accurate measurement of this parameter are getting attention. Prior to the determination of machine capability, qualifying the measurement system is necessary by a Gage R&R (repeatability and reproducibility) study to decide if the system is appropriate for measuring the particular parameter. This qualification should not be confused with the calibration procedure of that equipment. In this chapter, the procedure of a Gage R&R study will be overviewed. Then, the measurement possibility of placement machine accuracy and the calculation of the machine capability index will be detailed.

[1.4.1 Gage R&R study]

Gage R&R (repeatability and reproducibility) study is intended for analyzing a measurement system, whether or not it suits measuring a given parameter. The repeatability characterizes the measurement equipment, i.e., estimates variation in measurements taken by a single person. Reproducibility describes the persons, who perform measurements, i.e., estimates the variation induced when different operators

measure the same items. The study uses more than one person/operator (typically 3), several items owning the parameter to be measured (usually up to 20), and some repeats of the measurements (typically 2–3). The study should be performed randomly in a single-blind experiment, meaning that the operators are blinded, that is, they do not know which part / which repeat actually they measure. After the experiment, the value of *R&R* can be calculated by analyzing variances with the following expression (1.16):

$$R\&R = \frac{\sigma^2_{measurement}}{\sigma^2_{total}} = \frac{\sigma^2_{repeatability} + \sigma^2_{reproducibility}}{\sigma^2_{repeatability} + \sigma^2_{reproducibility} + \sigma^2_{item}} \tag{1.16}$$

If the value of *R&R* is below 10–15%, then the measurement system is qualified for measuring the given parameter. If the *R&R* is higher than 30%, the measurement system is not appropriate for the specific measurement. In between, further actions should be taken, like analyzing if the variance between operators was significant, then training of the operators or upgrading the measurement system.

If the parameter to be measured follows a normal distribution with high certainty, then the variances in (1.16) can be estimated as follows. Consider an R&R study with *o* operators, *p* repeats of measurements, and *q* items. Determine the repeatability firstly. The range of measurement repeats (*Rmr*) should be calculated for each operator and for each item (1.17).

$$Rmr_{i,k} = \max(mes_{i,1,k};...;mes_{i,p,k}) - \min(mes_{i,1,k};...;mes_{i,p,k}) \tag{1.17}$$

where $mes_{i,j,k}$ is the j^{th} measurement result by a given operator (i) for a given item (k) within the repeats (p). Then, the average of *Rmr* values is calculated for each operator separately, resulting in $\overline{Rmr_i}$ for the i^{th} operator (1.18).

$$\overline{Rmr_i} = \frac{\sum_{k=1}^{q} Rmr_{i,k}}{q} \tag{1.18}$$

Next, the average of $\overline{Rmr_i}$ values is determined (1.19).

$$\overline{\overline{Rmr}} = \frac{\sum_{i=1}^{o} \overline{Rmr_i}}{o} \tag{1.19}$$

Note that (1.18) and (1.19) could be contracted to one expression, but usually, they are calculated separately because of illustration purposes. The standard deviation and thus, the variance of repeatability can be estimated then by dividing (1.19) with a so-called coefficient d_2, resulting in (1.20). The respective coefficient can be obtained from the Table of Control Chart Constants (Table. 1.6) [1.39]. The value of d_2 depends on the subgroup size (n), which is equal to the number of measurement repeats (p) in this case; e.g., $d_2 = 1.128$ if the value of measurement repeats is 2.

*** Insert Table 1.6 ***

Caption: 1.6. The d_2 values for estimating the standard deviation

Credit: [1.39]

n	2	3	4	5	6	7	8	9	10	11	12	13
***d*₂**	1.128	1.693	2.059	2.326	2.534	2.704	2.847	2.970	3.078	3.173	3.258	3.336
n	14	15	16	17	18	19	20	21	22	23	24	25
***d*₂**	3.407	3.472	3.532	3.588	3.640	3.689	3.735	3.778	3.819	3.858	3.895	3.931

$$\sigma_{repeatability} = \frac{\overline{\overline{Rmr}}}{d_{2\,|n=p}} \tag{1.20}$$

For determining the reproducibility, the average of measurement repeats (*Xmr*) should be calculated for each operator and for each item (1.21).

$$\overline{Xmr_{i,k}} = \frac{\sum_{j=1}^{p} mes_{i,j,k}}{p} \tag{1.21}$$

where $mes_{i,j,k}$ is the j^{th} measurement result by a given operator (i) for a given item (k) within the repeats (p). Then, the average of $\overline{Xmr_{i,k}}$ values is calculated for each operator separately, resulting in $\overline{\overline{Xmr_i}}$ for the i^{th} operator (1.22).

$$\overline{\overline{Xmr_i}} = \frac{\sum_{k=1}^{q} \overline{Xmr_{i,k}}}{q} \tag{1.22}$$

Next, the range of $\overline{\overline{Xmr_i}}$ values is determined (1.23).

$$R_{\overline{\overline{Xmr}}} = \max(\overline{\overline{Xmr_1}}; ...; \overline{\overline{Xmr_o}}) - \min(\overline{\overline{Xmr_1}}; ...; \overline{\overline{Xmr_o}}) \tag{1.23}$$

The standard deviation and thus, the variance of reproducibility can be estimated then by dividing (1.23) with the respective coefficient d_2, resulting in (1.24). The subgroup size (n) is equal to the number of operators (o) in this case, e.g., $d_2 = 1.693$ if the number of operators is 3.

$$\sigma_{reproducibility} = \frac{R_{\overline{\overline{Xmr}}}}{d_{2\,|n=o}} \tag{1.24}$$

Finally, the standard deviation of the measured item parameter should be calculated. The average of each and every measurement (all measurement repeats and all operators) for a particular item should be averaged first. Since the average of measurement repeats

has already been calculated, it is enough averaging the values of $\overline{Xmr_{i,k}}$ for each item separately, resulting in $\overline{\overline{Xim_k}}$ for the k^{th} item (1.25).

$$\overline{\overline{Xim_k}} = \frac{\sum_{i=1}^{o} \overline{Xmr_{i,k}}}{o} \tag{1.25}$$

Next, the range of $\overline{\overline{Xim_k}}$ values is determined (1.23).

$$R_{\overline{\overline{Xim}}} = \max(\overline{\overline{Xim_1}}; ...; \overline{\overline{Xim_q}}) - \min(\overline{\overline{Xim_1}}; ...; \overline{\overline{Xim_q}}) \tag{1.26}$$

The standard deviation and thus, the variance of the items' parameter can be estimated then by dividing (1.26) with the respective coefficient d_2, resulting in (1.27). The subgroup size (n) is equal to the number of items (q) in this case, e.g., $d_2 = 3.078$ if the number of measured items is 10.

$$\sigma_{item} = \frac{R_{\overline{\overline{Xim}}}}{d_{2|n=q}} \tag{1.27}$$

Finally, the variances should be determined for obtaining the R&R value (1.16) by calculating the squares of the respective standard deviations ($\sigma_{repeatability}, \sigma_{reproducibility}, \sigma_{item}$).

[1.4.2 Measuring component placement position]

For determining the machine capability index of component placement machines, an experiment should be carried out. In this, many components (e.g., 1 000 pcs. of passive discrete resistors) are placed onto a test board. There are several parameters, which can be varied in the experiment – e.g., size of component (for example 0603 or 0201), type of placement nozzle (or the sequential number of nozzles on a collect&place head),

orientation of a nozzle (0°, 90°, 180°, 270°) – and the machine capability index can be determined for each variant.

A specific test board should be used, which allows the measurement of component positions after placement. The test board includes reference marks (fiducial points), and the corners of passive components are measured to the marks for determining the component positions (Fig. 1.34). The positional- and rotational offset of a particular component can be calculated then by using (1.28) – (1.30) [1.40].

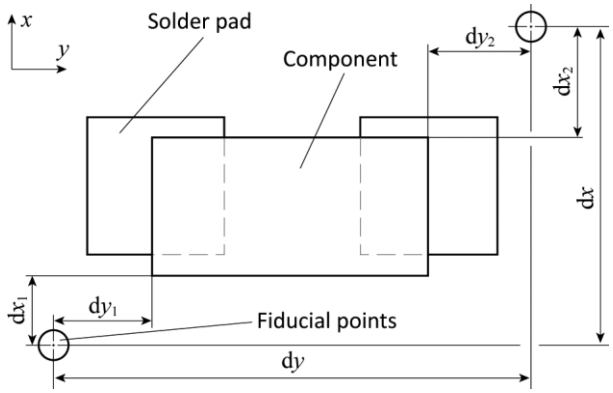

*** Insert Figure 1.34 ***

Caption: 1.34. Test pattern for measuring the component location after placement

Credit: –

$$x_{offset} = \frac{\mathrm{d}\,x_1 - \mathrm{d}\,x_2}{2} \tag{1.28}$$

$$y_{offset} = \frac{\mathrm{d}\,y_1 - \mathrm{d}\,y_2}{2} \tag{1.29}$$

$$\theta_{offset} = \arctan\left(\frac{\mathrm{d}\,x}{\mathrm{d}\,y}\right) - \arctan\left(\frac{\mathrm{d}\,x - \mathrm{d}\,x_1 - \mathrm{d}\,x_2}{\mathrm{d}\,y - \mathrm{d}\,y_1 - \mathrm{d}\,y_2}\right) \tag{1.30}$$

There are two kinds of measurement principles, namely absolute measurement and relative measurement. In the case of absolute measurement, the corners of all components are measured to the same reference marks at the corners of the printed wiring board

(global fiducial points). Contrary, in the case of the relative measurement method, reference marks are designed onto the test board around each component locations (local fiducial points), and the corners of components are always measured to the respective (closest) reference marks. At the absolute measurement method, the accuracy of measuring equipment (e.g., coordinate measuring machine) plays a key role in the measurement error since usually large distances should be measured between the component corners and the reference marks. In the case of the relative measurement method, much shorter distances should be measured; the primary cause of the measurement error is the accuracy/inaccuracy of the test pattern. For example, if a footprint for a given component has a slight positional offset, a placement offset will be measured even then if the respective component is placed into an absolutely proper position. Test boards, which are designed for the relative measurement method, are prepared, therefore, with vacuum technology using a glass substrate. After measuring the components position, the average and the standard deviation can be calculated for the lateral and rotational offsets assuming that the process of component placement follows a normal distribution.

[1.4.3 Machine and process capability index]

Machine and process capability indices are the quantitative measures regarding how those can perform against specifications. The process or machine output parameter, which is described by the capability index, is assumed following a normal distribution. The capability index actually merges the two parameters of the normal distribution (mean: $\hat{\mu}$ and standard deviation: $\hat{\sigma}$) into one single parameter by comparing the

measured process parameters to a theoretical three sigma process. The limits of that theoretical process are the upper and lower specification limits (*USL* and *LSL*), and *T* is the target value (Fig. 1.35).

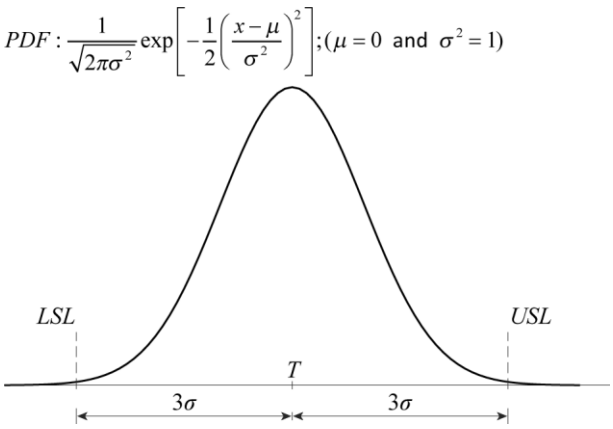

*** Insert Figure 1.35 ***

Caption: 1.35. The probability density function of normal distribution

Credit: –

The process capability ($\hat{C}_p$) and machine capability ($\hat{C}_m$) indices can be calculated by (1.31) for processes and machines where the mean of measured parameter equals to the value of a target ($\hat{\mu} = T$):

$$\hat{C}_{p,m} = \frac{USL - LSL}{2 \cdot k \cdot \hat{\sigma}} \tag{1.31}$$

where *USL* and *LSL* are the specification limits, *k* is 3 for process capability, and 4 for machine capability, and $\hat{\sigma}$ is the standard deviation of the measured process parameter. The typical specification limits for component placement are the one-quarter of the component shorter side. For example, the shorter side of a 0603 size resistor is 750 µm; the *USL* and *LSL* are then +187 µm and –187 µm, respectively. In some cases (e.g., high-quality electronics), stricter rules can also be applied like ±100 µm for this component

size. Usually, a $\hat{C}_{p,m}$ value larger than 1 ($\pm 3\sigma$ process) is accepted, whereas a too large value of $\hat{C}_{p,m}$ may indicate unnecessary precision that might be expensive.

If the mean of measured parameter is not equal to the value of a target ($\hat{\mu} \neq T$), i.e., the mean is not centered between the specification limits, then the corrected capability index ($\hat{C}_{pk,mk}$) is calculated by (1.32). Note that $\hat{C}_{pk,mk} \leq \hat{C}_{p,m}$.

$$\hat{C}_{pk,mk} = \min\left[\frac{USL - \hat{\mu}}{k \cdot \hat{\sigma}}; \frac{\hat{\mu} - LSL}{k \cdot \hat{\sigma}}\right] \tag{1.32}$$

where $\hat{\mu}$ is the mean of the measured parameter.

By knowing the capability index of a parameter, the fallout or defect rate of that parameter can be estimated. Multiplying the capability index by 3, the interval width regarding the variation of that parameter can be obtained; e.g., if the capability index is 1.33, then the interval width is $\pm 4\sigma$. The coverage by this interval (area under the PDF – Probability Density Function), or more precisely, the probability that a parameter lies between $\mu - n\sigma$ and $\mu + n\sigma$ is given by (1.33) [1.39]:

$$p = P(\mu + n\sigma) - P(\mu - n\sigma) = \Phi(n) - \Phi(-n) = \mathrm{erf}\left(\frac{n}{\sqrt{2}}\right) \tag{1.33}$$

where erf is the Gauss error function (1.34) [1.39]:

$$\mathrm{erf}(x) = \frac{2}{\sqrt{\pi}} \int_{\xi=0}^{\xi=x} e^{-\xi^2} d\xi \tag{1.34}$$

The process fallout, defect rate is usually represented in part per million (ppm); typical ppm values for capability indices are collected in Table 1.7.

*** Insert Table 1.7 ***

Caption: 1.7. Defect rate in ppm for specific capability indices

Credit: –

$\hat{C}_{p,m}$	**Interval width**	**Area under PDF** $p = \Phi(n) - \Phi(-n)$	**Defect rate in PPM** $(1-p)\cdot 10^6$
0.33	$\pm 1\sigma$	0.682689492137086	317 311
0.66	$\pm 2\sigma$	0.954499736103642	45 500
1.00	$\pm 3\sigma$	0.997300203936740	2 700
1.33	$\pm 4\sigma$	0.999936657516334	63
1.66	$\pm 5\sigma$	0.999999426696856	0.6
2.00	$\pm 6\sigma$	0.999999998026825	0.002

In the long term, parameters can shift significantly; therefore, these defect rates are usually estimated also for a maximum allowed 1.5σ shift (Table 1.8) to take the real-life increase in parameter variation into account. Note that a $\pm 6\sigma$ process shifted by 1.5σ is not equal to a $\pm 4.5\sigma$ process, because the mean is not centered within the specification limits. Therefore the ppm is calculated in this case slightly differently (1.35); defects beyond the far specification limit (opposite to the direction of shift) are omitted:

$$(1-p)\cdot 10^6 / 2 \qquad (1.35)$$

*** Insert Table 1.8 ***

Caption: 1.8. Defect rate in ppm in the case of a 1.5σ shift in the parameter

Credit: –

$\hat{C}_{p,m}$	**Sigma levels (1.5σ shift)**	**Area under PDF** $p = \Phi(n) - \Phi(-n)$	**Defect rate in PPM** $(1-p)\cdot 10^6 / 2$
1.00	1.5σ	0.866385597462284	66 807
1.33	2.5σ	0.987580669348448	6 210
1.66	3.5σ	0.999534741841929	233
2.00	4.5σ	0.999993204653751	3.4

[1.5 Reflow soldering]

As mentioned in Chapter 1.2, after populating the printed wiring board with components, the assembly travels through an oven, where the solder alloy in the solder paste is reflowed. The methods for heating the assembly include infrared radiation (Chapter 2), forced convection (Chapter 3), or vapor phase soldering (Chapter 4). The molten, liquid state solder wets the metalized terminals and forms the solder joints (fillet shape). Then, the assembly is cooled down, the solder solidifies and establishes the mechanical and electrical connection between the components and the printed wiring board. The most critical factor in this step from the assembly quality and reliability point of view, the heating profile (reflow profile) will be presented. Besides, phenomena happening during the soldering like component shift or intermetallic layer formation will be discussed in this chapter. Finally, some reflow failures, soldering defects will be presented briefly.

[1.5.1 Reflow soldering profile]

The reflow soldering profile is the temperature curve over the duration of assembly soldering. It influences not just the quality of the assembly (whether or not soldering defects will occur), but the reliability as well through influencing the intermetallic compound formation within the joint. There are two types of reflow soldering profiles, linear profile (delta type) and soak profile (trapezoidal type). Acquiring temperature profiles by thermocouples is detailed in Chapter 2. The soak profile can be divided into four-five sections (phases), as illustrated in Fig. 1.36.

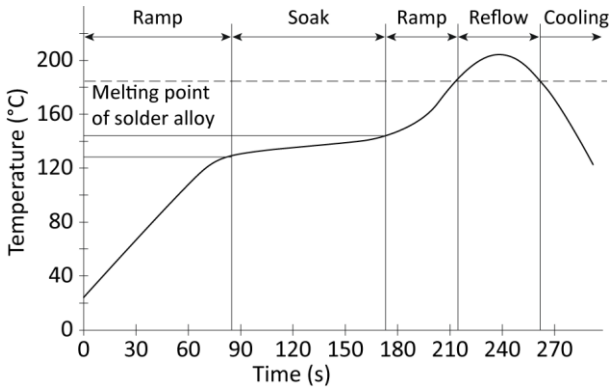

*** Insert Figure 1.36 ***

Caption: 1.36. Typical soak reflow profile

Credit: –

The first phase of the profile (ramp) is a rapid heating up to 120–150 °C. This is followed by a soak phase, where the flux in the solder paste is activated, and the temperature distribution over the assembly is homogenized. The ramp and the soak phases together are also called as pre-heating. Then, the next main phase is the reflow of the solder, where the optimal peak temperature depends on the melting point of the alloy. For example, the melting point of the Sn63/Pb37 alloy is 183 °C, whereas that of the lead-free Sn96.5/Ag3/Cu0.5 alloy is 217–219 °C. The peak temperature of the profile is set to 20–30 °C higher than these melting points. The reflow phase can follow the soak phase immediately, or a separate ramp phase can be inserted in between. Lastly, the assembly is cooled down with a pre-defined rate (cooling phase). The typical parameters of the phases in reflow profiles are collected in Table 1.8 with indicative values. Note that all the solder paste manufacturers have specific recommendations regarding these parameters for their pastes and alloys.

*** Insert Table 1.9 ***

Caption: 1.9. Typical reflow parameters

Credit: –

Phase in reflow profile	SnPb	SnAgCu
Ramp	Temperature range: 0–150 °C Rate of heating: <2 °C/s Duration: 60–150 s	Temperature range: 0–150 °C Rate of heating: <2 °C/s Duration: 60–150 s
Soak	Temperature range: 150–183 °C Duration: 60–90 s	Temperature range: 150–183 °C Duration: 60–90 s
Reflow	Peak temperature: 208–220 °C Duration: 45–90 s	Peak temperature: 208–220 °C Duration: 45–90 s
Cooling	Down to 130 °C Rate of cooling: 3–4 °C/s	Down to 130 °C Rate of cooling: 3–4 °C/s

The reflow phase in the temperature profiles is characterized regularly by two parameters. Since components with different heat capacities can heat up with different rates, a difference in temperature (ΔT) might exist in the peak temperature (Fig. 1.37). The ΔT should be below 5 °C based on industrial standards, and its value is much more critical for lead-free assemblies, where the peak temperature should be above ~240 °C and should not be higher than ~255 °C at each and every component. A ΔT too large can cause the damage of the components and/or the substrate (including conductive traces) and also can contribute to the excessive warpage of the printed wiring board.

An inappropriate set of the reflow profile parameters can cause various reflow soldering failures. A too low rate of temperature change in the phase of the ramp can cause the slump of the solder paste (paste viscosity would decrease), resulting in the formation of solder bridges. Contrary, a too fast rate of heating would cause the boiling of flux, and particles in the solder paste can be ejected due to excessive outgassing. These solder balls can form short circuits between the leads of fine-pitch components.

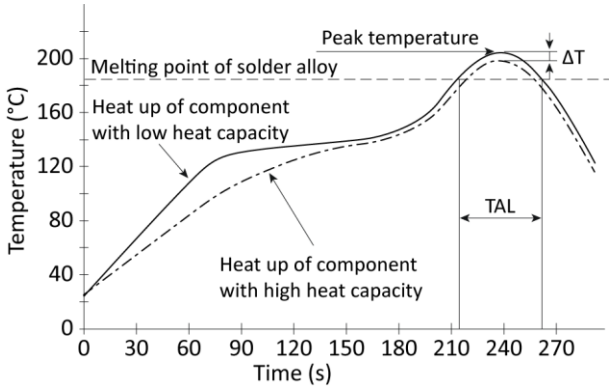

*** Insert Figure 1.37 ***

Caption: 1.37. Parameters for characterizing the reflow phase of the thermal profile

Credit: –

The incorrect parameter set of the soak phase can result in a temperature difference too large between low and high heat capacity components, thus increasing the ΔT also. A soak too short can cause insufficient activation of the flux, resulting in excessive oxidation on the metallization and yielding solder wetting problems. A soak too long can also cause excessive oxidation and reduces the throughput of the manufacturing line.

A peak temperature too low would result in brittle “cold” joints, whereas a peak temperature too high would damage the temperature-sensitive components. The other parameter is the time above liquidus (TAL). An appropriate length of this time is necessary for the solder joint formation, but a TAL too long would cause excessive oxidation during the soldering, resulting in quality and reliability issues.

The stage of cooling influences considerably the structure of solder joints and thereby the quality and reliability of joints. A cooling too rapid can cause the cracking of components besides. In the case of high silver content (> 2.8% wt%) solder alloys, a cooling rate too slow can contribute to the formation of shrinkage defect (Chapter 1.5.2).

The linear-type reflow profile has a similar shape to the soak-type profile; the difference is that the phase of soak is omitted. This shorter profile can increase the throughput of the manufacturing line. The disadvantage of linear-type profiles is the possibly higher ΔT in the peak temperature. So, this profile is recommended for not too complex assemblies.

During soldering, two phenomena occur mainly. On the one hand, the solder wets the component metallization by the energy of surface tension. On the other hand, an intermetallic layer will form at the solder-pad interface because of diffusion. Both phenomena and the respective parameters (surface tension and diffusion) depend strongly on the temperature and on the duration of the reflow phase. For addressing these phenomena, a new measure, the "heating factor" has been introduced recently to characterize this part of the reflow profile more precisely than that by the peak temperature and TAL. The heating factor is the area under the curve of the temperature profile in the phase of reflow (Fig. 1.38), and it is defined by (1.36) [1.41].

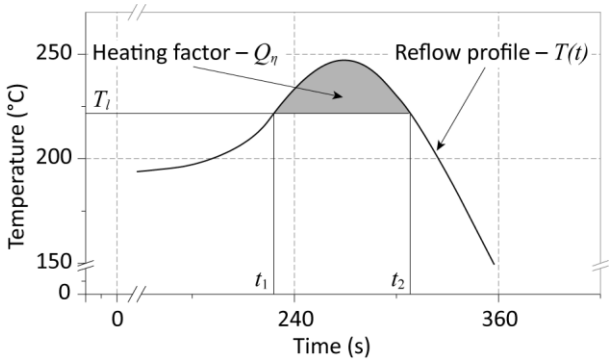

*** Insert Figure 1.38 ***

Caption: 1.38. Representation of the heating factor

Credit: –

$$Q_\eta = \int_{t_1}^{t_2} \left(T(t) - T_l\right) \mathrm{d}t\,, \tag{1.36}$$

where Q_η is the heating factor [K·s], $T(t)$ is the measured temperature, t_1 is the onset of solder alloy melting, $(t_2 - t_1)$ is the time above liquidus, and T_l is the melting point of the alloy.

[1.5.2 Intermetallic layer formation]

Intermetallic compounds (IMC) inherently form during soldering because of diffusion. Usually, the compounds precipitate in the solder bulk, and at the solder-pad interface are differentiated. Intermetallic compounds precipitating at the solder-pad interface grow the intermetallic layer (IML). The properties of this layer essentially affect the quality and reliability of solder joints. The thickness of the intermetallic layer depends mainly on the reflow profile (Q_η factor), on the solder alloy, and on the pad- and component metallization. If the surface finish on the printed wiring board presents in the form of a thin layer (e.g., immersion tin, immersion silver, OSP), then the main compound of the intermetallic layer is Cu_6Sn_5 (Fig. 1.39) [1.42].

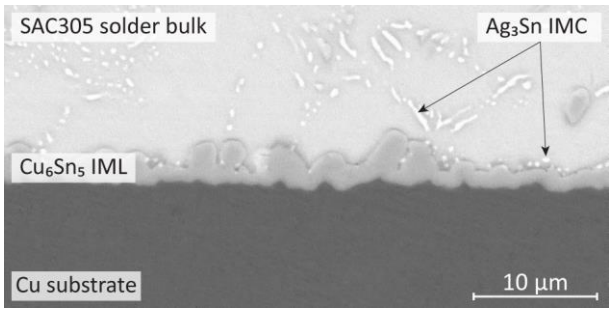

*** Insert Figure 1.39 ***

Caption: 1.39. Intermetallic compound formation during soldering

Credit: [1.42]

Appropriate thickness, in this case, is ~2 and ~4 μm for lead-bearing and for lead-free solder alloys. The intermetallic layer is thicker for lead-free alloys because of the high tin content and of the high value of the Cu-Sn interdiffusion coefficient. If the surface finish of the printed wiring board is the so-called ENIG (electroless nickel and immersion gold), the main composition of the intermetallic layer will be Ni_3Sn_4, and the thickness of the intermetallic layer will be lower, 1–2 μm due to the lower value of Ni-Sn interdiffusion coefficient. The thickness of the intermetallic layer should lie between these values. When the layer thickness is smaller than a critical value, fractures can occur inside the solder joint easily. The strength of solder joints increases with increasing reflow time, because Cu_6Sn_5 intermetallic compounds also precipitate in the solder bulk, strengthening the joint structure. If the thickness of the intermetallic layer increases beyond a critical value, there is an onset of a brittle fracture in the IMC layer, resulting in decreased strength with reflow time.

A simple, diffusion limited model for estimating the average of intermetallic layer thickness (or the rate of growth during soldering) includes the root of time (duration for intermetallic formation), and the temperature dependency by Arrhenius's law (1.37).

$$x(mm) = x_0 + t^n \cdot k_0 e^{\left(-\frac{E_a}{RT}\right)} \tag{1.37}$$

where x_0 is the initial layer thickness, which is practically zero by the process of soldering, but has a specific value if the layer growth is examined when carrying out aging tests, like high-temperature storage life (HTSL) tests. In (1.37), t is the time, and n is an exponent with a value lower than 1. The typical values for n are 0.3 and 0.5 for liquid-solid diffusion (e.g. soldering) and for solid-solid diffusion (e.g. HTSL test), respectively. Similarly, parabolic growth kinetics (n = 0.5) applies, when the layer growth

is controlled by the volumetric diffusion; and subparabolic growth kinetics ($n = 0.3$) applies, when the layer growth is controlled by grain boundary diffusion [1.43]. E_a is the activation energy ($J \cdot mol^{-1}$), R is the universal gas constant, T is the absolute temperature, and k_0 is a pre-exponential factor. It is common in electronics that the activation energy is expressed in electron-volt [eV]. In this case, the Boltzmann constant (k_B) should be used instead of R, with the value (and with the unit) of $8.617 \cdot 10^{-5}$ [$eV \cdot K^{-1}$]. During the soldering, the growth rate of Cu_6Sn_5 (η phase) is more pronounced than that of the Cu_3Sn (ε phase). Oppositely, the growth rate of the ε phase is usually larger during life-time tests. Nevertheless, e.g., Krammer et al. showed that the ε phase readily grows during soldering, but its thickness reaches only approximately 200 nm [1.42]. As an example, the element map of an intermetallic layer over a TEM (transmission electron microscope) Darkfield image is presented in Fig. 1.40.

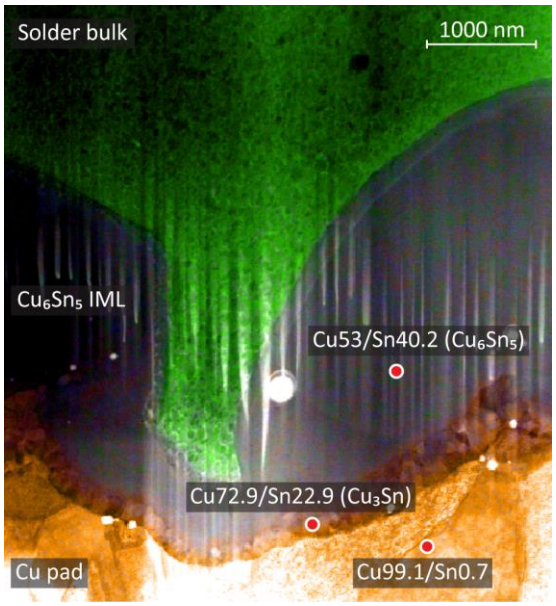

*** Insert Figure 1.40 ***

Caption: 1.40. The intermetallic layer formed during soldering

Credit: [1.42]

It can be observed in Fig. 1.39 and Fig. 1.40 that the shape, the microstructure of the intermetallic layer is usually not simply layer-type, but scallop-type. For describing the intermetallic layer growth, more specific models than the simple one in (1.37) exist also.

According to the review of Tu et al., the growing mechanism of the Cu_6Sn_5 intermetallic layer (IML) can be described by two mass fluxes [1.44]. One of them is the diffusion of Cu atoms through the valley between every two scallops. The other flux is the so-called ripening reaction among the scallops. The growth equation was given as (1.38) [1.44]:

$$r^3 = \int \left(\frac{\gamma \Omega^2 D C_0}{3 \mathrm{N_A} L \mathrm{R} T} + \frac{\rho A \Omega v(t)}{4\pi m N_p(t)} \right) \mathrm{d}t \,, \tag{1.38}$$

where r is the radius of an average size scallop, γ is the surface energy of the scallop, Ω is the average atomic volume, D is the atomic diffusivity in the molten solder, C_0 is the solubility of Cu in the molten solder, $\mathrm{N_A}$ is the Avogadro's number, L is the numerical relating the mean separation between scallops and the mean scallop radius, R is the Boltzmann coefficient, T is the absolute temperature, ρ is the density of Cu, A is the total area of the solder/Cu interface, v is the consumption rate of Cu in the reaction, m is the atomic mass of Cu, N_p is total number of scallops at the interface. In the equation, the first term is the interfacial reaction term, while the second term is the ripening term.

According to the findings of Krammer et al., the intermetallic layer structure depends on the silver content of the solder alloy [1.42]. High Ag-content alloys form a more layer-type IML, whereas it is more scallop-type in low Ag-content alloys after the soldering. In their experiment, at high silver-content solder alloys, the ratio between the reaction term and the ripening term was shifted toward the reaction term due to the higher number of scallops (higher N_p). Contrary, in the case of low Ag-content solders, the ratio between

the reaction term and the ripening term shifted toward the ripening term because of the lower number of scallops.

The rate of intermetallic layer growth during soldering and life-time tests is also affected significantly by the silver content in the solder alloy. Silver forms the Ag_3Sn intermetallic compound with tin during soldering, and this intermetallic compound precipitates around the primary β-Sn dendrites. The Ag_3Sn intermetallic compounds can adsorb on the surface of the Cu_6Sn_5 intermetallic layer, and they can obstruct the growing of that layer [1.45]. If the silver content in the solder is higher – especially in the case of alloys with hypereutectic silver compositions (>2.7 wt%) – more Ag_3Sn IMC can adsorb, and thus lower intermetallic layer can form. The different rate of intermetallic layer thickness growth during Thermal Shock tests between low- and high silver-content alloys can be explained by the different extent of grain-boundary diffusion [1.46]. Krammer et al. showed that the number of grain boundaries along a unit of length correlates with the rate of intermetallic layer growth, and a higher number of grain boundaries were found at high silver-content alloys than at low silver-content ones [1.42] (Fig. 1.41).

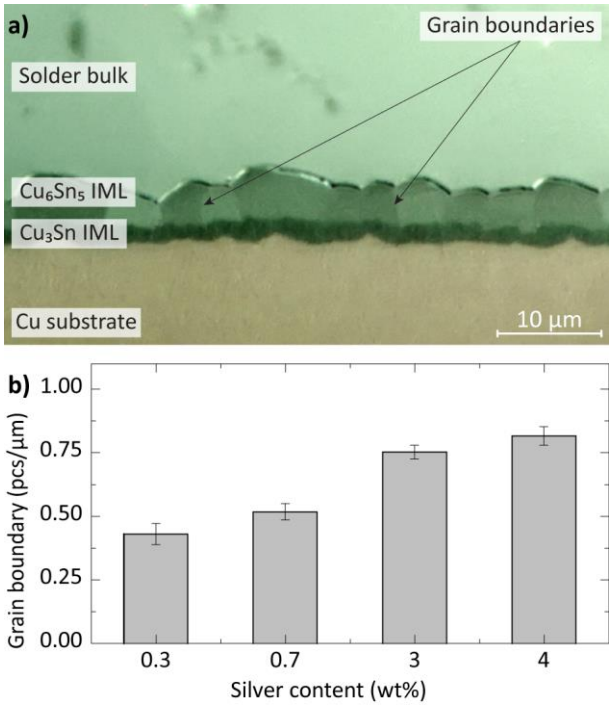

*** Insert Figure 1.41 ***

Caption: 1.41. Grain boundaries in the solder joint: a) polarised optical image of a low-silver content joint cross-section; b) the specific amount of grain boundaries over silver content

Credit: [1.42]

Finally, the silver content in the alloy affects both the quality and reliability of solder joints by the differing development of Ag_3Sn intermetallic compounds as the function of the cooling rate during soldering. Generally, three types of Ag_3Sn compounds morphology can be found: particle-like, needle-like, and also plate-like. The sequential evolution or modification of Ag_3Sn compounds during a decreasing cooling rate is usually particle-like → needle-like → plate-like [1.47]. These plate-like Ag_3Sn IMCs are very brittle, and during the cool-down phase of the reflow, they can initiate cracks in the solder joints and can result in the so-called shrinkage defect [1.48]. Additionally, they can

promote crack propagation along their boundary during the life-time of electronic circuits, thus reducing their reliability [1.49].

If the silver content in the solder is low, there will be less Ag_3Sn IMC inside; the large Ag_3Sn plates may effectively be minimized by using SnAgCu alloys with hypoeutectic silver compositions of approximately 2.7 wt% or below [1.50]. The difference can be observed by comparing Fig. 1.39 and Fig. 1.42. Therefore, besides the cost reduction, the decrease of silver content can have a positive effect on the quality of solder joints as well. However, the application of such reduced silver solder compositions in SnAgCu alloys will require careful evaluation with respect to their thermomechanical fatigue properties [1.51].

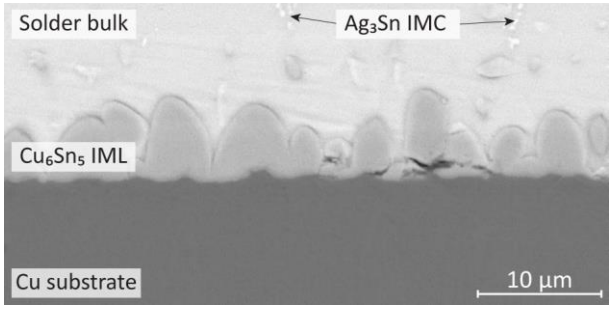

*** Insert Figure 1.42 ***

Caption: 1.42. Structure of a low silver-content (~0.3% wt%) solder joint

Credit: [1.42]

[1.5.3 Component movements during reflow soldering]

During soldering, forces acting on electronic components include the surface tension and the hydrostatic force exerted by molten solder. In the case of large-scale components (e.g., DPAK packages), inhomogeneity in temperature may results in inhomogeneity in the surface tension force, causing component skewing and/or open joint formation. A

similar problem (the so-called “tombstone” effect) can arise if there is a difference in the onset of solder melting between the opposite sides of two-terminal components. In this case, one end of the component is lifted by the torque arising at the opposite side, where the solder is already in the molten state. This phenomenon can cause the formation of open joints. Contrary, the forces arising during soldering can also aid in eliminating soldering failures. If a surface-mounted resistor or a capacitor is misplaced by the component placement machine, the surface tension force can restore the component to its central position; this phenomenon is called component self-alignment.

The first force models, which investigated the component movements during reflow soldering, were two-dimensional and mainly focused on the tombstone effect [1.52]. The model of Wassinkg and Werguld [1.52] assumed that there was no solder on the opposite face of the component, and it considered the solder fillet as a straight line instead of a curve. In addition, the model, due to its simple manner, did not take the hydrostatic pressure of the liquid solder into consideration. A more complex model has been described by Ellis and Masada [1.53], which took the hydrostatic and capillary pressure of the molten solder into account and considered the solder fillet as a curve. However, it was also a two-dimensional model like the Wassink-Verguld model. The model comprised further simplifications; it assumed that the component is brick-shaped (i.e., rectangle in 2D), and its mass center was in the geometrical center of the body. Also, the model presumed that the corner of the component was always in contact with the soldering surface (pad), and it rotated around that point. Though, the model included many specific details – the meniscus of the solder was not considered to be a straight line, the force due to hydrostatic pressure was taken into consideration, and the chip

component was allowed to be displaced along its pad length to illustrate the effect of component misplacements.

Next, Krammer presented a three-dimensional force model for addressing the component movements during reflow soldering [1.54]. Based on that model, mainly five forces are acting on the chip components during reflow soldering (Fig. 1.43.). The force originating from surface tension ($\vec{F}_{st}$) is acting on the boundary contact line of the three phases, which are the solder, gas, and component metallization. The forces originating from hydrostatic ($\vec{F}_h$) and from capillary ($\vec{F}_c$) pressure are acting on the area of the component metallization, while the force originating from dynamic friction ($\vec{F}_v$) depends on the mass of the liquid solder, which should be actuated. The fifth force is due to the gravitational acceleration ($\vec{F}_g$) if there is no solder, for example, at the opposite side and dynamic friction between component and pad metallization should be calculated.

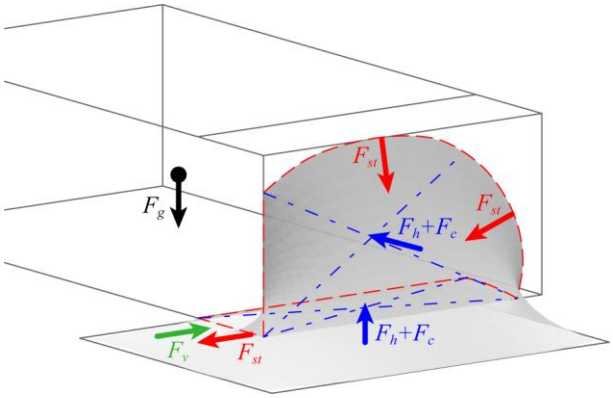

*** Insert Figure 1.43 ***

Caption: 1.43. Forces acting during solder on a component misplaced parallel to its shorter side

Credit: [1.54]

In the case of component misplacements (which are due to the placement machine inaccuracy), the main force promoting the self-alignment is originating from the surface tension of the liquid solder. The surface tension force acts on the appointment place of the three phases. In general case, the appointment place of a three-phase system is a space curve, which is called the contact line in soldering technologies. Therefore, the net force originating from the surface tension can be obtained by integrating the term of surface tension (γ_{LG}) along the contact line (1.39) [1.54]:

$$\vec{F}_{st} = \int_{v} \gamma_{LG} \mathrm{d}\vec{l} \tag{1.39}$$

The forces, originating from hydrostatic- and capillary pressures of the molten solder, push the component out from the solder. These forces are acting on the vertical face- and bottom side metallization of the component, as illustrated in Fig. 1.43 ($F_h + F_c$). The capillary pressure is the pressure difference between the two sides of a curved liquid surface, and that pressure drop across the fillet (ΔP) can be determined by the Laplace's equation. Therefore, the force originating from hydrostatic- and capillary pressures (F_p) can be determined by integrating the pressure along the surface of the component metallization (1.40) [1.54]. However, this is a generalized expression, and in reality, the force due to capillary pressure does not act on the component but balances the change in hydrostatic pressure over the curved liquid surface based on the theorem of pressure continuity.

$$\vec{F}_{p} = \int_{A_{cs}} \rho_s g \cdot h(\vec{r})\, \mathrm{d}\vec{S} + \int_{A_{cs}} \left\{ \gamma_{LG} \left(\frac{1}{r_1(b(\vec{r}))} + \frac{1}{r_2(b(\vec{r}))} \right) \right\} \mathrm{d}\vec{S}\,, \tag{1.40}$$

where A_{cs} is the surface of component metallization, ρ_s is the density of molten solder, $\vec{r}$ is the spatial vector, $h(\vec{r})$ is the height of liquid column, which is infinitesimally close to

the point designated by the vector $\vec{r}$ on the surface A_{cs}, $b(\vec{r})$ is the point on top of the liquid column, where the capillary pressure can be calculated.

The dynamic friction between liquid and solid phases slows the movement of components. The force originating from the dynamic friction between a solid and a liquid phase can be described by the Newton Viscous Force equation [1.55]. The liquid (molten solder) can be considered as a series of horizontal layers. The top layer in the molten solder is infinitesimally close to the bottom side metallization of component, and its velocity is equal to the speed of the component movement. The velocity of the bottom layer is 0, equivalent to the speed of the pad. Thus, the decelerating force due to dynamic friction is (1.41) [1.54]:

$$\vec{F}_v = \int_{A_{cs}} \frac{\eta_s \cdot (\vec{v} - \vec{v}_0)}{d(\vec{r})} \mathrm{d}S \tag{1.41}$$

where η_s is the viscosity of the molten solder, $\vec{v}$ is the speed vector of component movement, $\vec{v}_0$ is the velocity of a point at d distance from the A_{cs} surface, which is zero if it is on the pad, and not zero if the point is located on the surface of the molten solder, $d(\vec{r})$ is the distance between the pad or the surface of the solder and the location under investigation, which is designated by vector $\vec{r}$ on surface A_{cs}.

For determining forces by the hydrostatic pressure and surface tension, the solder profile should be known, it should be calculated. Two main methods are available for determining the solder profile; one is based on the principle of pressure continuity, while the other one is based on minimizing the energy originating from the surface tension and the potential energy due to gravity.

The principle of pressure continuity claims that in a static liquid, no pressure gradients exist horizontally, and the pressure in the vertical direction changes proportionally to the distance from the liquid surface (i.e., proportionally to the height of liquid column) [1.53]. Consequently, since the fillet profile decreases in height as a function of the distance from the chip component, a continuously changing pressure difference must exist along the curve of profile. Generally, Laplace's equation is used to relate the pressure drop (ΔP) and the fillet surface geometry. In its most general form, the equation is (1.42).

$$\Delta P = \gamma \cdot \left(\frac{1}{r_1} + \frac{1}{r_2} \right) \tag{1.42}$$

where r_1 and r_2 are the radii of curvature of the fillet measured normal to the surface of the component face metallization. For two-dimensional models, the solution is (1.43) [1.53].

$$\frac{\mathrm{d}^2 y}{\mathrm{d}x^2} = \frac{1}{\gamma} \left(\rho g y - \Delta P_0 \right) \cdot \left[1 + \left(\frac{\mathrm{d}y}{\mathrm{d}x} \right)^2 \right]^{3/2} \tag{1.43}$$

where γ is the surface tension coefficient, while ΔP_0 is $P_{solder} - P_{atmosphere}$.

Equation (1.43) is a second-order nonlinear differential equation, which solution defines the fillet profile. Once the correct profile is known, the points at which the surface tension forces and pressure forces act can be computed. In this approach, two boundary conditions are needed (i.e., the solder wets until the end of the pad, and the height of the solder fillet is equal to the height of the component), and ΔP_0 is an unknown. The problem that for a three-dimensional force model, this principle cannot be used because the equation system would be too complex.

Calculating the solder profile by minimizing the energy rests on that the equilibrium shape of a liquid meniscus at a liquid-gas phase boundary of a system – in which solid, liquid, and gaseous phases coexist – is given by the balance of forces acting on the system. In the case of reflow soldering, the liquid phase is the molten solder, the solid phases are the soldering surfaces (component metallization and pad), while the gaseous phase is the atmosphere of the reflow oven altered by the evaporation of flux. When the boundary condition is that the solder wets until the end of the metallization (the contact angle depends on the volume of the solder), the energy of the system which should be minimized is given by equation (1.44) [1.56]:

$$E = E_S + E_G \tag{1.44}$$

where E_S is the energy originating from the surface tension (1.45) [1.57]:

$$E_S = \int_A \gamma \mathrm{d}S \tag{1.45}$$

and E_G is the potential energy due to gravity (1.46) [1.58]:

$$E_G = \iiint_{x\ y\ z} \rho \cdot g \cdot z \cdot \mathrm{d}x\mathrm{d}y\mathrm{d}z \tag{1.46}$$

where γ is the surface tension coefficient, ρ is the solder density, g is the gravitational acceleration, A is the surface of solder fillet.

When the boundary condition is set in a way that the end of the pad is not reached by the solder (which is very common for lead-free solders), then the contact angle is equal to the wetting angle. In this case, the energy term due to the surface tension can be determined by the following. At first, divide the surface of the solder into three parts; A_0, A_1, and A_2 for indicating the surface on the liquid-gas boundary and the surface of the liquid-solid boundaries, respectively (Fig. 1.44).

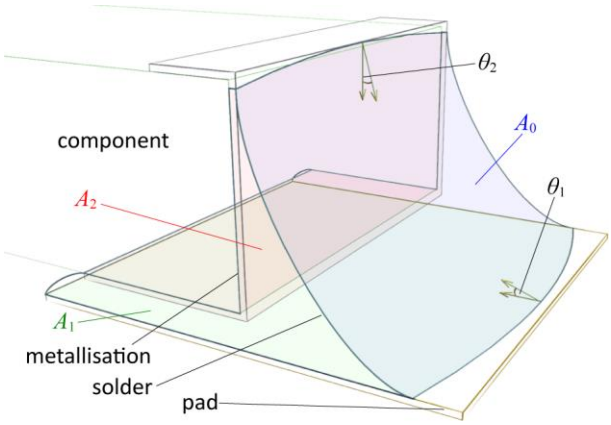

*** Insert Figure 1.44 ***

Caption: 1.44. Boundary condition that the solder does not reach the end of the metallization

Credit: [1.54]

Then, the energy originating from the surface tension forms as (1.47):

$$E_S = \int_{A_0} \gamma_{LG} \mathrm{d}S + \int_{A_1} \gamma_{LS_1} \mathrm{d}S + \int_{A_2} \gamma_{LS_2} \mathrm{d}S \,, \tag{1.47}$$

where γ_{LG} is the surface tension coefficient between the liquid-gas boundary and γ_{LSi} is the surface tension coefficient between the liquid-solid boundary.

Besides, the Young equation claims that in a static liquid, the balance between the surface tensions is the following (1.48):

$$\gamma_{LS} = \gamma_{SG} - \gamma_{LG} \cdot \cos\theta \tag{1.48}$$

By substituting (1.48) into (1.47) and by omitting the zero value terms, the following equation can be obtained (1.49) [1.59]:

$$E_S = \int_{A_0} \gamma_{LG} \mathrm{d}S + \int_{A_1} -\gamma_{LG} \cdot \cos\theta_1 \mathrm{d}S + \int_{A_2} -\gamma_{LG} \cdot \cos\theta_2 \mathrm{d}S \,, \tag{1.49}$$

where: A_0 is the boundary area of the solder and the gas, A_1 is the boundary area of the solder and the pad, A_2 is the boundary area of the solder and the component metallization,

θ_1 is the wetting angle on the contact line of solder and pad, and θ_2 is the wetting angle on the contact line of solder and component metallization. Minimizing the energy term (1.44) can be performed by various methods and software tools, e.g., by numerical modeling and by gradient descent method applied in the so-called tool Surface Evolver [1.60].

[1.6 Pin-in-paste technology]

Through-hole components cannot be substituted entirely by surface-mounted ones, and they are used even today, mainly on two application areas. On the one hand, the mechanical strength of through-hole joints can be larger than that of surface-mounted joints by even one order of magnitude. Therefore, connectors in high-reliability devices are still used in the through-hole form. On the other hand, the continuous decrease in the size of surface-mounted components leads to the problem that heat dissipation became constrained to a smaller area, thereby reducing the power capacity of small factor surface-mounted components. This implies that through-hole components are used still in power electronics, and for high current applications.

The traditional mass soldering method for through-hole components is the so-called wave soldering. This technology needs 200–300 kg of solder to be heated up to 280–300 °C, thus requiring a large amount of energy. Omitting this technology and using reflow soldering technology for both the surface-mounted and through-hole components would, therefore, be beneficial from the energy consumption and environmental implication points of view. That is why the reflow soldering of through-hole components (pin-in-paste technology) started spreading in the early 2000s. This raised two requirements against the through-hole components: they should withstand the peak temperature of reflow soldering (up to 250 °C) and should be packed in a form that component placement machine can handle them.

[1.6.1 Steps of pin-in-paste technology]

The steps of pin-in-paste technology are quite similar to the steps of reflow soldering technology. The only difference is the apertures that are opened (formed) also for through-hole components in the stencil (Fig. 1.45).

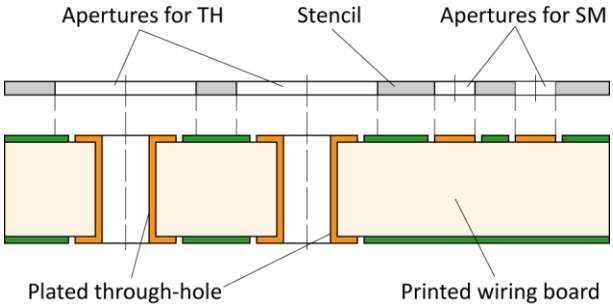

*** Insert Figure 1.45 ***

Caption: 1.45. Stencil for pin-in-paste technology

Credit: –

During stencil printing, the solder paste fills the through-holes in a given extent depending on the printing speed, on the squeegee attack angle, and on the through-hole diameter (Fig. 1.46). The through-hole filling of solder paste affects significantly the quality and reliability of the finally formed solder joints. Thus its value is carefully designed (Chapter 1.6.2) and controlled in this technology.

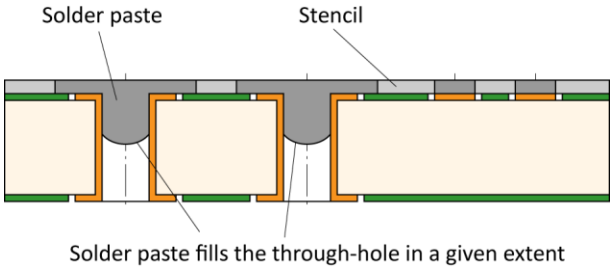

*** Insert Figure 1.46 ***

Caption: 1.46. Pin-in-paste technology – stencil printing

Credit: –

As a next step, the components are placed with automatic placement machines. Special placement heads (like DIP insertion heads) are used for the through-hole components occasionally, but in many cases, the same kind of nozzles can be used for both TH and SM components. The leads of the through-hole components tear the solder paste in the plated hole and push a part of the paste to the bottom side (Fig. 1.47). Under optimal conditions, this part of the solder paste will form the bottom side meniscus and will wet back to the plated hole during reflow soldering.

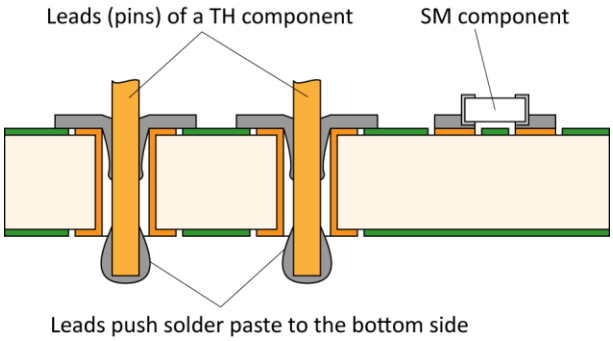

*** Insert Figure 1.47 ***

Caption: 1.47. Pin-in-paste technology – component placement

Credit: –

Lastly, the solder joints are formed by the same process as in traditional reflow soldering; the assembly is heated up above the melting point of the solder alloy, the solder wets the components' metallization and forms the solder joints (Fig. 1.48).

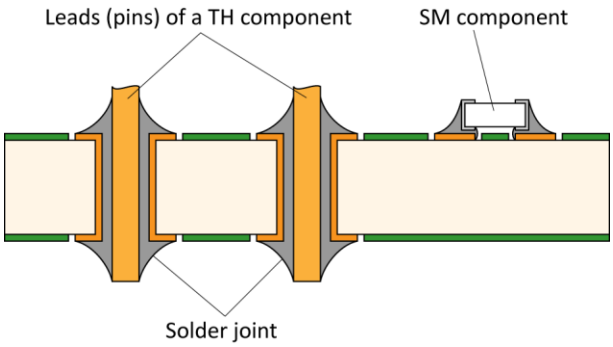

*** Insert Figure 1.48 ***

Caption: 1.48. Pin-in-paste technology – soldering

Credit: –

Care should be taken that, on the one hand, a larger amount of solder paste is necessary for through-hole components than for surface-mounted ones. On the one hand, the hole-filling by the solder paste (Fig. 1.46) cannot be inspected by SPIs (solder paste inspection machines). Thus, pin-in-paste technology demands much tighter control of the process of stencil printing. Actually, the lack of possibility for inline, 100% inspection of hole-filling exhibits the biggest disadvantage of pin-in-paste technology. Only offline inspection is possible by utilizing X-ray machines with tilted detectors.

[1.6.2 Calculating solder paste volume for pin-in-paste technology]

Determining the optimal amount of solder paste for soldering through-hole components by pin-in-paste technology is the critical step from the electronic devices' quality and reliability point of view. Especially, because the 100% inspection of solder pastes deposited for the TH components is not feasible at the moment. Zarrow was the first who described the necessary solder paste volume for pin-in-paste technology. He

took the volume of solder within the plated through-hole and the shrinkage factor of the solder paste into account (1.50) [1.61]:

$$P_{volume} = \frac{1}{S}\pi \cdot h \ \ r_{hole}{}^{2} - r_{lead}{}^{2} \tag{1.50}$$

where S is the shrinkage factor, h is the thickness of the Printed Circuit Board, r_{hole} is the radius of the plated-hole and r_{lead} is the radius of the component lead. The shrinkage factor of the solder paste is regularly 0.5, since half of the volume is flux, and only half of the volume contributes to the solder joint formation. This expression underestimates the necessary volume, because the volume of solder fillet (defined by the solder meniscus) is neglected.

A more appropriate expression was given by Coleman, which also took the volume of the solder fillet into account (1.51) [1.62]:

$$P_{volume} = \frac{1}{S}\left[\pi \cdot h \ \ r_{hole}{}^{2} - r_{lead}{}^{2} \ \ + 2 \cdot 0.215 \cdot r_{fillet}{}^{2} \cdot 2\pi \ \ 0.2234 \cdot r_{fillet} + r_{lead} \ \right] \tag{1.51}$$

This expression assumes that the solder wets the lead of the component exactly to the height, as the distance of the lead from the edge of the pad (r_{fillet}), as illustrated in Fig. 1.49. Furthermore, it assumes that the fillet is defined by a quarter arc of a circle, and the volume of the fillet is calculated by using Pappus's second centroid theorem [1.63]. This theorem claims that assuming that the rotating plane curve does not cross the axis, the solid's volume is equal to the length of the circle described by the plane curve's centroid multiplied by the area of the plane curve. Though (1.51) defines the necessary volume more precisely than (1.50), it is still a rough approximation. The fillet of a typical solder joint is more convex than a quarter arc of a circle (Fig. 1.49 – dashed line), and the wetting angle is always higher than 0°, e.g., 22° for a Sn96.5Ag3Cu0.5 alloy.

Consequently, (1.51) underestimates the volume of the fillet and thereby also the volume of the solder paste necessary for TH components in pin-in-paste technology.

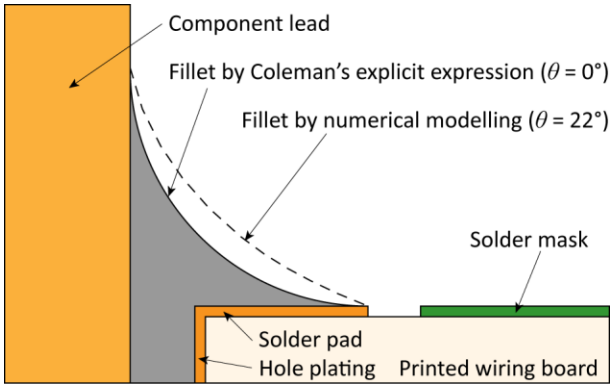

*** Insert Figure 1.49 ***

Caption: 1.49. Solder profiles by Coleman's expression, and by numerical modeling (θ is the wetting angle)

Credit: –

For obtaining the precise volume of solder joint for through-hole components, profile calculations can be performed by numerical modeling, which was mentioned in Chapter 1.5.3, and correction factors might be determined for Coleman's expression. The appropriate solder paste volume for through-hole components can be determined then by multiplying Coleman's expression with these factors. As an example, Krammer et al. determined correction factors considering both circular and square cross-section leads and various fillet radiuses [1.64]. Based on their calculations, the correction factor is (1.52) [1.64]:

$$C_{circle} = 1.523 - 0.125 \cdot r_{fillet} + 0.1335 \cdot r_{lead}$$
$$C_{square} = 1.243 + 0.1241 \cdot r_{fillet} - 0.006 \cdot edge\_length_{lead} \quad (1.52)$$

The amount of solder paste, which should be pushed into the plated holes, is determined then, by subtracting the volume of stencil aperture from the necessary volume. Regularly, the hole-filling of the solder paste should be around 50%.

[1.6.3 Controlling the solder paste deposition for pin-in-paste technology]

The quality and reliability of pin-in-paste technology are greatly affected by the hole-filling of the solder paste. Both too low and too large amounts of solder paste can result in the formation of voids within the solder joints or in an insufficient wetted area by the solder on pads (solder rings). The hole-filling by the solder paste can be influenced by the stencil design and by the process parameters of stencil printing. If the diameter of a plated hole is too large (e.g., twice the diameter than the thickness of printed wiring board), the hole-filling by solder paste can usually be also greater than the predefined value. In this case, the solder paste at the bottom side (pushed through by the component lead) might not wet back to the plated hole and can fall down from the lead or can remain at the end of the lead. The condition of solder wet-back can be described by the balance of two forces (1.53), the force due to surface tension, and by the gravity force.

$$F_{grav} = \rho V g \quad << \quad F_{sruf.tens.} = 2\pi r \cdot \gamma_{LG\cdot} \cos\theta \tag{1.53}$$

where ρ is the density of solder (~7 300 kg/m^3 for lead-free solders), V is the volume of solder pushed to the bottom side by the lead of through-hole component (note that the volume of solder is the half of the volume of paste because of shrinkage), g is the gravitational acceleration, r is the radius of component lead, γ_{LG} is the surface tension of solder (~550 mN/m for lead-free alloys), and θ is the wetting angle.

For appropriate solder wet-back, the force due to surface tension should be much larger. For this purpose, volume *V* should be reduced, which can be achieved by stencil webbing, i.e., by designing crosses into the apertures (Fig. 1.50). With this design, the hole-filling by solder paste can effectively be reduced.

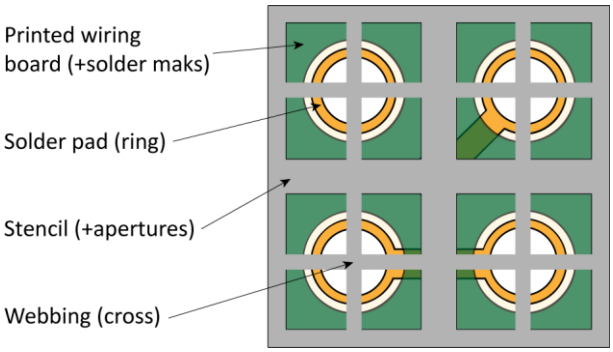

*** Insert Figure 1.50 ***

Caption: 1.50. Stencil webbing (designing crosses into apertures) for reducing the hole-filling by solder paste in pin-in-paste technology

Credit: –

If the diameter of a plated hole is too small (e.g., half the diameter than the thickness of the printed wiring board), the hole-filling by solder can be insufficient. In this case, preform solders (pre-shaped, fluxless solders) or step stencils can be used. Step stencils exhibit selective increment in thickness (~25–75 μm) at specific areas either on the top (squeegee) or the bottom (contact) side of stencil-foil. The thicker areas are located typically at the apertures for through-hole components or similarly at the apertures for ceramic BGA packages. The design rules for step stencils are overviewed in the standard of IPC-7525 [1.65]. It suggests a minimum distance (keep-out rule K_1 = 36 · *step_thickness*), which should be kept between a stencil aperture and the stencil-step so that the difference in the stencil levels does not result in printing failures. The standard

defines that the same design rules apply for both types of step stencils; either the step is formed on the squeegee side or on the contact side. However, keep-out rule K_1 is only a rough estimation for stencils with steps on their bottom side because neither the thickness nor the material of stencil foil is taken into consideration. These parameters affect the deformation of stencil loaded by the squeegee during printing, and determine whether or not a stencil can bend down completely to a solder pad, which is located nearby to the edge of a stencil step (Fig. 1.51).

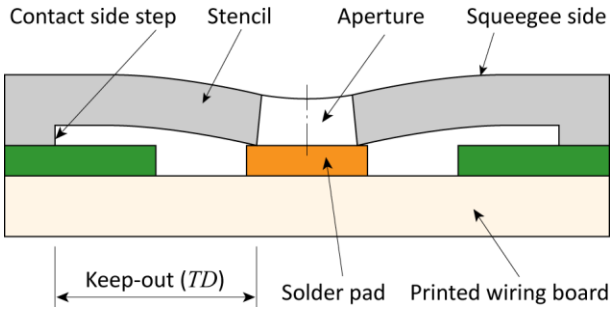

*** Insert Figure 1.51 ***

Caption: 1.51. Keep-out distance (*TD*) necessary for achieving complete stencil contact with the solder pad

Credit: –

Krammer et al. investigated the stencil deformation during stencil printing for determining keep-out rules for stencils with steps on the contact side [1.37]. FEM simulations were carried out in their work by varying differences in stencil levels (step heights: 0–90 µm) and stencil foil thicknesses (75–150 µm). Based on their results (Fig. 1.52), the necessary keep-out distance is much larger than that recommended by the standard of IPC7525. They also found that in the range of difference of 0–60 µm, the specified keep-out distance is nearly linearly proportional to the step height and to the foil

thickness (1.54) [1.37]. Note that the results of this investigation are valid for the generally used specific printing force of 0.3 N/mm.

$$TD = C \cdot h \cdot d \tag{1.54}$$

where *TD* is the necessary keep-out distance (mm), *C* is a coefficient of 1.6 (μm^{-1}), *h* is the stencil step height (µm), and *d* is the stencil foil thickness (µm).

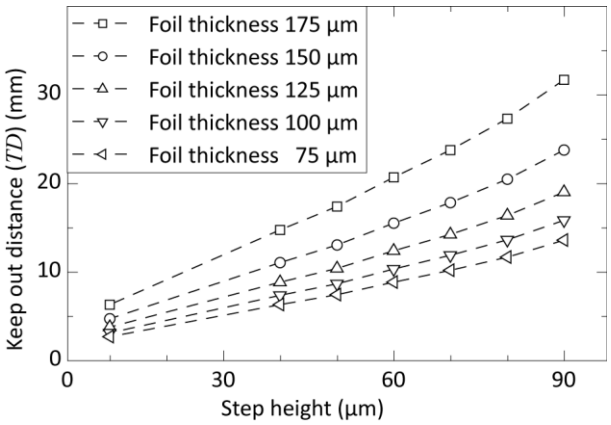

*** Insert Figure 1.52 ***

Caption: 1.52. Keep-out distances (*TD*) as a function of step height and stencil foil thickness

Credit: [1.37]

Process parameters of stencil printing also affect the hole-filling of solder paste in pin-in-paste technology. The optimization of the respective parameters, e.g., printing speed can be performed by numerical modeling, or recently even by utilizing machine learning techniques. Martinek et al. analyzed various machine learning-based methods for predicting hole-filling in pin-in-paste technology [1.66]. The analyzed methods included the following: artificial neural networks (ANN) trained by Bayesien Regularization or by Levenberg–Marquardt method; adaptive neuro-fuzzy inference systems (AFNIS) with Gaussian and Triangular input membership functions; gradient boosted decision trees.

They validated the prediction methods by measuring the hole-filling of solder paste at different printing speeds (20–70 mm/s) and at different hole diameters (0.8, 1.0, 1.1, 1.4 mm). The measurements were carried out by utilizing side-view X-ray images about the hole-filling of solder pastes (Fig. 1.53).

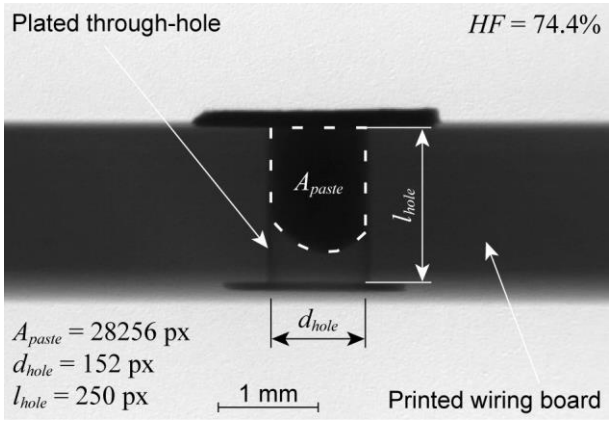

*** Insert Figure 1.53 ***

Caption: 1.53. Calculating the hole-filling in X-ray images (image resolution: 6.2 μm/px; through-hole diameter: 942 μm)

Credit: [1.66]

They analyzed then the prediction capability of investigated methods both for complete data set and for incomplete data sets [1.66]. The latter means that given measured input parameter values were completely excluded from the training data, and the corresponding predicted values of hole-filling were compared to the measured values. The excluded values in 4 different test scenarios were the following: excluding all data with a hole diameter of 1.0 mm; excluding all data with a hole diameter of 1.1 mm; excluding all data with a printing speed of 40 mm/s; excluding all data with a printing speed of 60 mm/s. This approach investigated the situation in manufacturing in a possible example, where the assembly of a new product was initiated, which product contained

completely different hole-diameters than the products have been assembled before. In the case of complete data sets, the error of the predicted hole-filling values compared to the measured ones, by calculating the mean of absolute percentage error (MAPE). They found that the machine learning techniques exhibited quite low values of error in the prediction; the average MAPE values were below 1.5–1.7% for all cases (Fig. 1.54).

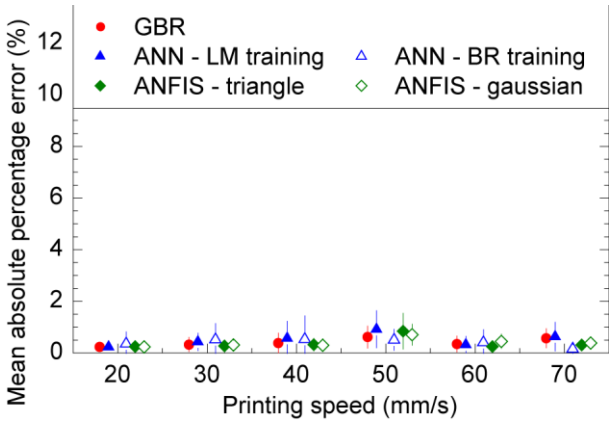

*** Insert Figure 1.54 ***

Caption: 1.54. Prediction errors for hole-diameter of 1.0mm over the printing speed – trained by the full data set

Credit: [1.66]

In the case of incomplete data sets, the MAPE values increased significantly, meaning that machine learning-based methods are sensitive for the prediction of values completely missing from the training data set. However, the performance was still acceptable in most cases (Fig. 1.55).

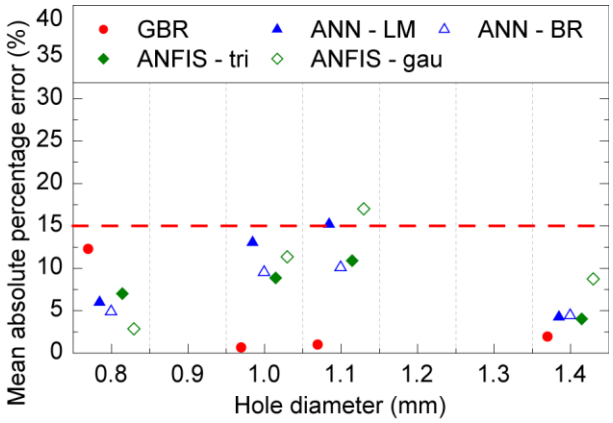

*** Insert Figure 1.55 ***

Caption: 1.55 Prediction errors for incomplete data set over the hole-diameter – printing speed of 40 mm/s was excluded from the training

Credit: [1.66]

After analyzing and optimizing all of the evaluated methods for their experiment, the ANN (artificial neural network) trained with BR (Bayesian Regularization) method provided the best results. This method was recommended by Martinek et al. for predicting the hole-filling in pin-in-paste technology [1.66]. In practice, the process parameters of PIP technology could be collected during the assembly even for all manufacturing lines in the concept of Industry 4.0, and the data can be fed-back to the design phase. By this, the design phase could be enhanced, engineering tasks for fine-tuning the process could be reduced or even eliminated, and the set-up time of manufacturing lines for new products could be shortened significantly.

[References Chapter 1]

[1.1] N.-C. Lee, Reflow Soldering Processes and Troubleshooting: SMT, BGA, CSP and Flip Chip Technologies, Newness, 2002.

[1.2] G. Harsányi, Elektronikai Technológia és Anyagismeret, University lecture notes, BME-ETT, 2019, ISBN: 978-963-421-791-6.

[1.3] C.S. Lau, M.Z. Abdullah, F.C. Ani, Effect of solder joint arrangements on BGA leadfree reliability during cooling stage of reflow soldering process, IEEE Transactions on Components, Packaging and Manufacturing Technology 2(12) (2012) 2098–2107.

[1.4] T. Plookphol, S. Wisutmethangoon, S. Gonsrang, Influence of process parameters on SAC305 lead-free solder powder produced by centrifugal atomization, Powder Technology 214 (2011) 506-512.

[1.5] W.Y.W. Yusoff, N. Ismail, N.S. Safee, A. Ismail, A. Jalar, M.A. Bakar, Correlation of microstructural evolution and hardness properties of 99.0Sn-0.3Ag-0.7Cu (SAC0307) lead-free solder under blast wave condition, Soldering & Surface Mount Technology 31(2) (2019) 102-108.

[1.6] O. Krammer, K. Dušek, Numerical investigation on the effect of the printing force and squeegee geometry on stencil printing, Journal of Manufacturing Processes 45(2019) 188-193.

[1.7] M. Hirman, F. Steiner, Optimization of solder paste quantity considering the properties of solder joints, Soldering & Surface Mount Technology 29(1) (2017) 15-22.

[1.8] T.N. Tsai, Modeling and optimization of stencil printing operations: a comparison study, Computers & Industrial Engineering 54(3) (2008) 374-389.

[1.9] IPC J-STD-005, Requirements for Soldering Pastes, Solder Paste Task Group (5-22b) of IPC, Bannockburn, Illinois, USA, 1995.

[1.10] J. Ferguson, Z. Kemblowski, Applied Fluid Rheology, Springer Netherlands, 1991, ISBN: 978-1-85166-588-4.

[1.11] O. Krammer, B. Gyarmati, A. Szilágyi, B. Illés, D. Bušek, K. Dušek, The effect of solder paste particle size on the thixotropic behaviour during stencil printing, Journal of Materials Processing Technology 262 (2018) 571-576.

[1.12] N.N. Ekere, D. He, L. Cai, The Influence of Wall Slip in the Measurement of Solder Paste Viscosity, IEEE Transactions on Components, Packaging and Manufacturing Technology 24(3) (2001) 468-73.

[1.13] H.A. Barnes, Measuring the viscosity of large-particle (and flocculated) suspensions — a note on the necessary gap size of rotational viscometers, Journal of Non-Newtonian Fluid Mechanics 94 (2000) 213-17.

[1.14] A. Pietriková, M. Kravčík, Boundary value of rheological properties of solder paste, 2011 34th International Spring Seminar on Electronics Technology (ISSE 2011), Tatranska Lomnica, Slovakia, (2011) 94-97.

[1.15] T.A. Nguty, N.N. Ekere, The rheological properties of solder and solar pastes and the effect on stencil printing, Rheologica Acta 39(6) (2000) 607-612.

[1.16] R. Durairaj, S. Mallik, N.N. Ekere, Solder paste characterisation: towards the development of quality control (QC) tool, Soldering & Surface Mount Technology 20(3) (2008) 34-40.

[1.17] G.P. Glinski, C. Bailey, K.A. Pericleous, A non-Newtonian computational fluid dynamics study of the stencil printing process, Proceedings of the Institution of Mechanical Engineers, Part C: Journal of Mechanical Engineering Science 215(4) (2001) 437-446.

[1.18] R. Durairaj, G.J. Jackson, N.N. Ekere, G. Glinski, C. Bailey, Correlation of solder paste rheology with computational simulations of the stencil printing process. Soldering & Surface Mount Technology 14(1) (2002) 11-17.

[1.19] T.I. Al-Ma'aiteh, O. Krammer, Non-Newtonian numerical modelling of solder paste viscosity measurement, Soldering & Surface Mount Technology 31(3) (2019) 176-180.

[1.20] J. Boyd, J.M. Buick, Analysis of the Casson and Carreau-Yasuda non-Newtonian blood models in steady and oscillatory flows using the lattice Boltzmann method", Physics of Fluids 19(9) (2007) 093103.

[1.21] J.W. Goodwin, R.W. Hughes, Rheology for chemists. An Introduction, 2nd edition, RSC Publishing, Cambridge, UK, 2008.

[1.22] S. Mallik, N.N. Ekere, A.E. Marks, A. Seman, R. Durairaj, Modelling of the timedependent flow behaviour of lead-free solder pastes used for flip-chip assembly applications, 2nd Electronics System-Integration Technology Conference (ESTC-2008), Greenwich, UK, (2008) 1219-1224.

[1.23] A. Pietriková, M. Kravcik, Investigation of rheology behavior of solder paste, 35th International Spring Seminar on Electronics Technology (ISSE 2012), Bad Aussee, Austria, (2012) 138-143.

[1.24] M. Holtzer, L. Nampo, Reducing print cycle time, SMT Magazine (October) (2015) 26-29.

[1.25] K.J. Vachaparambil, G. Mårtensson, L. Essén, Rheological characterization of non-Brownian suspensions based on structure kinetics, Soldering & Surface Mount Technology 30 (1) (2018) 57-64.

[1.26] R. Durairaj, S. Ramesh, S. Mallik, A. Seman, N.N. Ekere, Rheological characterisation and printing performance of Sn/Ag/Cu solder pastes, Materials Design 30 (2009) 3812-3818.

[1.27] W. Pabst, Fundamental considerations on suspension rheology, Ceramics − Silikáty 48(1) (2004) 6-13.

[1.28] S.S. Zhang, Y.J. Zhang, H.W. Wang, Effect of particle size distributions on the rheology of Sn/Ag/Cu lead-free solder pastes, Materials Design 31 (2010) 594-598.

[1.29] X. Bao, N.C. Lee, R.B. Raj, K.P. Rangan, A. Maria, Engineering solder paste performance through controlled stress rheology analysis, Soldering & Surface Mount Technology 10(2) (1998) 26-35.

[1.30] B. Illés, I. Bakó, Numerical study of the gas flow velocity space in convection reflow oven, International Journal of Heat and Mass Transfer 70 (2014) 185-191.

[1.31] B. Illés, A. Géczy, A. Skwarek, D. Busek, Effects of substrate thermal properties on the heat transfer coefficient of vapour phase soldering, International Journal of Heat and Mass Transfer 101 (2016) 69-75.

[1.32] V.N. Constantinscu, Laminar Viscous Flow, Springer-Verlag, New-York, 1995, ISBN: 978-1-4612-8706-3.

[1.33] S.H. Mannan, N.N. Ekere, I. Ismail, M.A. Currie, Flow processes in solder paste during stencil printing for SMT assembly, Journal of Materials Science: Materials in Electronics 6(1) (1995) 34-42.

[1.34] D. Riemer, Analytical engineering model of the screen printing process: Part I. Solid State Technology August (1988) 107-111.

[1.35] D. Riemer, Analytical engineering model of the screen printing process: Part II. Solid State Technology September (1988) 85-90.

[1.36] W.S. Seo, J.B. Kim, Filling analyses of solder paste in the stencil printing process and its application to process design, Soldering & Surface Mount Technology 25(3) (2013) 145-154.

[1.37] O. Krammer, L.M. Molnár, L. Jakab, A. Szabó, Modelling the effect of uneven PWB surface on stencil bending during stencil printing process, Microelectronics Reliability 52(1) (2012) 235-240.

[1.38] O. Krammer, L. Jakab, B. Illes, D. Bušek, I.B. Pelikánová, Investigating the attack angle of squeegees with different geometries, Soldering & Surface Mount Technology 30(2) (2018) 112-117.

[1.39] A.M. Joglekar, Statistical Methods for Six Sigma, John Wiley & Sons, 2003, ISBN: 0-471-20342-4.

[1.40] IPC-9850, Surface mount placement equipment characterization, Developed by the SMT Component Placement Equipment Subcommittee (5–41) of the Assembly Equipment Committee (5–40) of IPC, July 2002.

[1.41] P.L. Tu, Y.C. Chan, K.C. Hung, J.K.L. Lai, Study of micro-BGA solder joint reliability, Microelectronics Reliability 41 (2001) 287-293.

[1.42] O. Krammer, T. Garami, B. Horváth, T. Hurtony, B. Medgyes, L. Jakab, Investigating the thermomechanical properties and intermetallic layer formation of Bi micro-alloyed low-Ag content solders, Journal of Alloys and Compounds 634 (2015) 156-162.

[1.43] D. Shangguan, Lead-Free Solder Interconnect Reliability, ASM International, USA, 2005, ISBN: 978-0-87170-816-8.

[1.44] K.N. Tu, K. Zeng, Tin-lead (SnPb) solder reaction in flip chip technology, Materials Science and Engineering 34 (2001) 1-58.

[1.45] L.C. Tsao, Evolution of nano-Ag3Sn particle formation on Cu–Sn intermetallic compounds of Sn3.5Ag0.5Cu composite solder/Cu during soldering, Journal of Alloys and Compounds 509 (2011) 2326-2333.

[1.46] M. Yang, M. Li, C. Wang, Interfacial reactions of eutectic Sn3.5Ag and pure tin solders with Cu substrates during liquid-state soldering, Intermetallics 25 (2012) 86-94.

[1.47] H.T. Lee, Y.F. Chen, T.F. Hong, K.T. Shih, Effect of Cooling Rate on Ag3Sn Formation in Sn-Ag Based Lead-Free Solder, 11th Electronics Packaging Technology Conference (EPTC 2009), Singapore, (2009) 875-878.

[1.48] E.F. Monlevade, W. Peng, Failure Mechanisms and Crack Propagation Paths in Thermally Aged Pb-Free Solder Interconnects, Journal of Electronic Materials 36(7) (2007) 783-797.

[1.49] D.W. Henderson, T. Gosselin, A. Sarkhel, Ag3Sn plate formation in the solidification of near ternary eutectic Sn–Ag–Cu alloys, Journal of Materials Research 17(11) (2002) 2775-2778.

[1.50] S.K. Kang, D.Y. Shih, D. Leonard, D.W. Henderson, T. Gosselin, S. Cho, J. Yu, W.K. Choi, Controlling Ag3Sn Plate Formation in Near-Ternary-Eutectic Sn-Ag-Cu Solder by Minor Zn Alloying, JOM, June (2004) 34-38.

[1.51] S.K. Kang, P. Lauro, D.Y. Shih, D.W. Henderson, J. Bartelo, T. Gosselin, S.R. Cain, C. Goldsmith, K. Puttlitz, T.K. Hwang, W.K. Choi, The Microstructure, Thermal Fatigue, and Failure Analysis of Near-Ternary Eutectic Sn-Ag-Cu Solder Joints, Materials Transactions 45(3) (2004) 695-702.

[1.52] R. Wassink, M. Verguld, Drawbridging of leadless components, Hybrid Circuits 9 (1986) 18-24.

[1.53] J.R. Ellis, G.Y. Masada, Dynamic behavior of SMT chip capacitors during solder reflow, IEEE Transactions on Components, Hybrids, and Manufacturing Technology 13(3) (1990) 545-52.

[1.54] O. Krammer, Modelling the self-alignment of passive chip components during reflow soldering, Microelectronics Reliability 54(2) (2014) 457-463.

[1.55] M.B. Abot, D.R. Basco, Computational Fluid Dynamics An Introduction for Engineers, Longman Scientific & Technical, Harlow, England, 1989.

[1.56] L.M. Racz, J. Szekely, Determination of Equilibrium Shapes and Optimal Volume of Solder Droplets in the Assembly of Surface Mounted Integrated Circuits, ISIJ International 33(2) (1993) 336-342.

[1.57] N.J. Nigro, S.M. Heinrich, A.F. Elkouh, X. Zou, R. Fournelle, P.S. Lee, Finite element Method for Predicting Equilibrium Shapes of Solder Joints, Transaction of ASME - Journal of Electronic Packaging 115 (1993) 141-146.

[1.58] N.J. Nigro, F.J. Zhou, S.M. Heinrich, A.F. Elkouh, R.A. Fournelle, P.S. Lee, Parametric Finite element Method for Predicting Shapes of Three-Dimensional Solder Joints, Transaction of ASME - Journal of Electronic Packaging 118 (1996) 142-147.

[1.59] X. Zhao, C. Wang, G. Wang, G. Zheng, S. Yang, An Integrated System for Prediction and Analysis of Solder Interconnection Shapes, IEEE Transaction on Electronics Packaging Manufacturing 23(2) (2000) 87-92.

[1.60] K. Brakke, Surface Evolver, available at: www.susqu.edu/brakke/evolver/evolver.html (accessed 19 September 2019).

[1.61] P. Zarrow, Reflow soldering of through-hole components, Journal of Surface Mount Technology 12(4) (1999), available at: www.smta.org/knowledge/journal_detail.cfm?ARTICLE_ID=19

[1.62] W.E. Coleman, D. Jean, J.R. Bradbury-Bennett, Stencil design for mixed technology through-hole/SMT placement and reflow, Soldering & Surface Mount Technology 12(3) (2000) 8-12.

[1.63] J.W. Harris, H. Stocker, Solids of rotation, Handbook of Mathematics and Computational Science, Springer-Verlag, New York, NY, 1998. 111-113.

[1.64] O. Krammer, B. Varga, K. Dušek, New method for determining correction factors for pin-in-paste solder volumes, Soldering & Surface Mount Technology, 29(1) (2017) 2-9.

[1.65] IPC-7525, Stencil Design Guidelines, Developed by the Stencil Design Task Group (5-21e) of the Assembly and Joining Process Committee of IPC; May 2000.

[1.66] P. Martinek, O. Krammer, Analysing machine learning techniques for predicting the hole-filling in pin-in-paste technology, Computers & Industrial Engineering 136 (2019) 187-194.